Probing the energy transfer dynamics of photosynthetic reaction center complexes through hole-burning and single-complex spectroscopy

by

Kerry Joseph Riley

A dissertation submitted to the graduate faculty in partial fulfillment of the requirements for the degree of

DOCTOR OF PHILOSOPHY

Major: Physical Chemistry

Program of Study Committee:
Ryszard Jankowiak, Co-Major Professor
Edward Yeung, Co-Major Professor
Yeon Kyun Shin
Xueyu Song
Hans U. Stauffer

Iowa State University

Ames, Iowa

2007

CHAPTER 1 – PHOTOSYNTHESIS OVERVIEW

1.1 The Photosynthetic Process – A Brief Introduction

Photosynthesis is the process by which light energy is used to drive reactions that generate sugars to supply energy for cellular processes. It is one of the most important fundamental biological reactions and occurs in both prokaryotic (e.g. bacteria) and eukaryotic (e.g. plants and algae) organisms. Photosynthesis is also remarkably intricate, requiring the coordination of many different steps and reactions in order to successfully transform absorbed solar energy into a biochemical usable form of energy. However, the net reaction for all photosynthetic organisms can be reduced to the following, deceptively general, equation developed by Van Niel [1]

$$H_2 - D + A \overset{h\nu}{\Rightarrow} A - H_2 + D$$

where H_2-D is the electron donor, e.g. H_20, H_2S. A is the electron acceptor, e.g. CO_2, and A-H_2 is the synthesized sugar. Amazingly, this simple net equation is responsible for creating the oxidizing atmosphere of Earth and the recycling of CO_2, both of which are necessary for the sustainment of our global ecosystem [1-3].

The intricate process needed to arrive at the above equation for photosynthesis can be broken down into four main phases: (1) light absorption and energy delivery by antenna systems, (2) primary electron transfer in reaction centers, (3) energy stabilization by secondary electron transfer, and (4) synthesis and transport of stable sugar products [2]. The first phase is a photophysical process, the second and third phases are photochemical processes, and the fourth phase is a biochemical process. This dissertation is primarily concerned with the first two phases, the photophysical and initial

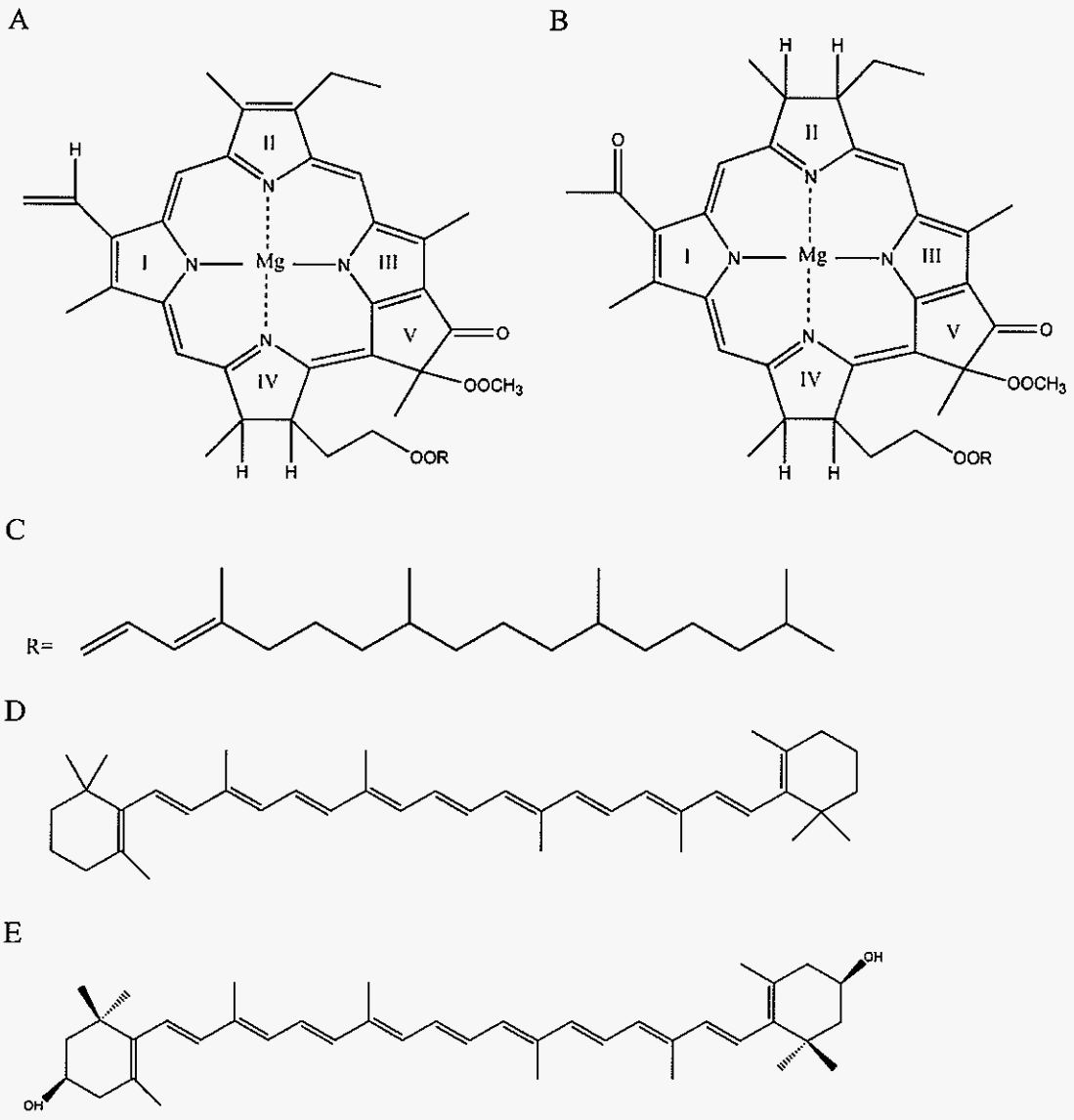

Figure 1. Chemical structures of (A) chlorophyll, (B) bacteriochlorophyll, (C) the phytyl tail, (D) beta-carotene, a carotenoid of photosystem II (PS II) which is responsible for quenching singlet states and preventing oxidation to the PS II RC, and (E) zeaxanthin, a xanthophyll which is an oxidized hydroxy derivative of beta-carotene, that is responsible for quenching reactive oxygen species in cyanobacterial and plant photosynthetic organisms. The phytl tail is abbreviated as R in structures (A) and (B). The Roman numbers I to V label the Chl and BChl rings according to the IUPAC nomenclature system. The structures of pheophytin and bacteriopheophytin are respectively identical to chlorophyll and bacteriochlorophyll, except that the central Mg atom is replaced with H atoms bonded to rings I and III.

This electron transfer proceeds by either one of two distinct mechanisms: (i) non-cyclic phosphorylation or (ii) cyclic phosphorylation [phosphorylation in this sense means the light driven synthesis of ATP from adenine diphosphate (ADP) and phosphate (P_i)] [1, 6]. Non-cyclic phosphorylation is oxygenic and occurs in cyanobacteria and higher plants. Cyclic phosphorlyation is anoxygenic and occurs in green sulfur and purple bacteria [2]. However, cyanobacteria and plants can undergo cyclic phosphorylation when they are too low in energy to run non-cyclic phosphorylation. The differences between cyclic and non-cyclic phosphorylation are outlined in Figs 3-4. Basically, in cyclic phosphorylation, the electron lost from the reaction center returns to re-reduce it. In non-cyclic phosphorylation, the electrons are not recycled; electrons must be obtained from an outside source, i.e. H_20, to re-reduce the oxidized reaction center. Non-cyclic phosphorylation is also different from cyclic phosphorylation in that a reducing compound, nicotinamide adenine dinucleotide phosphate (NADPH), is produced along with ATP.

Consequently, the fourth phase uses the ATP and NADPH generated by the third phase in carbon fixation, which generates sugars that the organism can use for energy. These are commonly referred to as the dark reactions of photosynthesis, since they can take place in the absence of light via the fact that the ATP and NADPH has already been generated by light reactions of photosynthesis. In oxygenic organisms, the dark reactions are referred to as the Calvin, Basshan, and Besson cycle, or Calvin cycle [1, 4], after the researchers who determined the chemistry of these enzymatic reactions. The Calvin cycle is responsible for CO_2 fixation into carbohydrates in oxygenic organisms. For

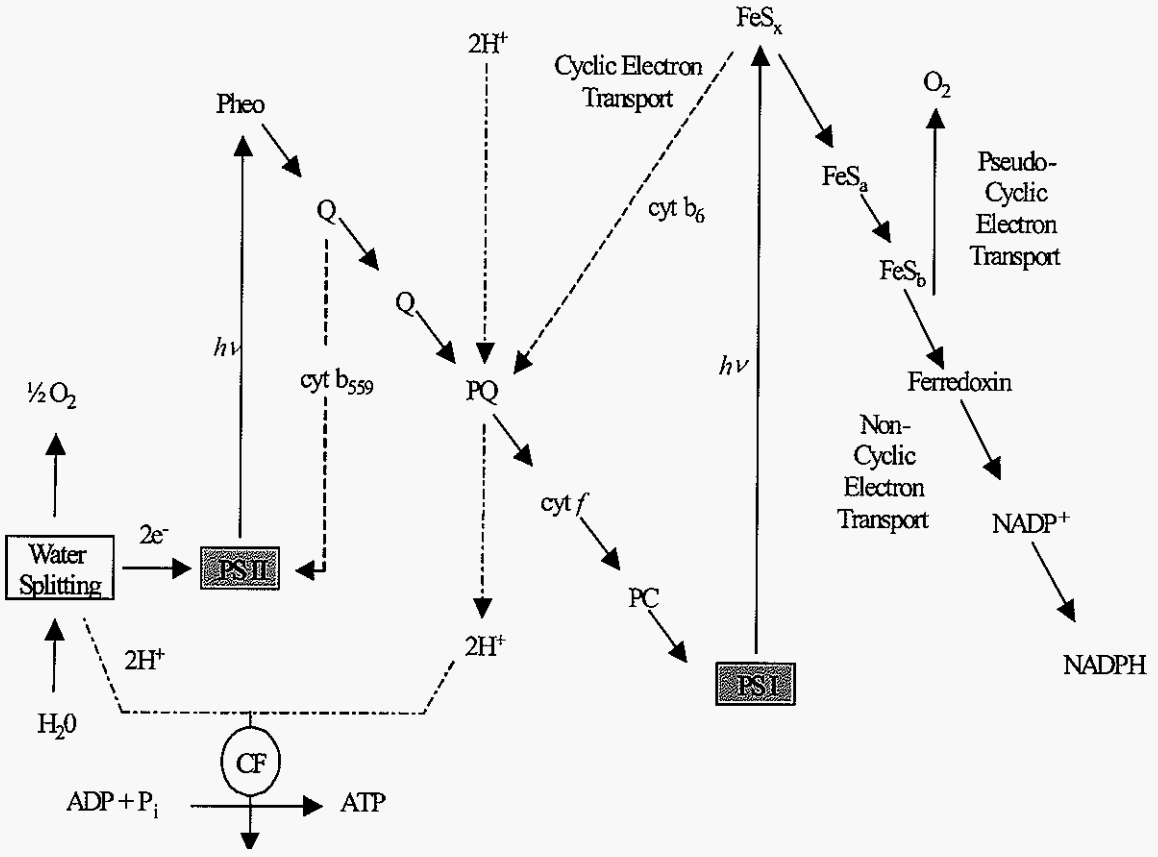

Figure 4. Schematic of non-cyclic phosphorylation in cyanobacteria and plants [1]. When the PS II RC is excited by ($h\nu$), primary electron transfer to pheophytin (Pheo) occurs, then is passed down to two quinones (Q), a plastiquinone (PQ), cytochrome *f* (cyt *f*), and to plastocyanin (PC). After excitation, the photosystem I (PS I) RC transfers an electron to a series of iron-sulfur complexes ($FeS_{x, a, b}$) and PS I is reduced by PC. Ferredoxin then reduces FeS_b, which is then reduced by NADP reductase ($NADP^+$), leading to the synthesis of NADPH and is used in the Calvin cycle. The PS II RC is reduced by H_2O (generating O_2) and cytochrome b_{559} (cyt b_{559}). Electron transfer across the thylakoid membrane creates a proton gradient, which drives ATP synthesis via the ATP synthase CF. If the organism is too low in NADPH to synthesize sugars, cyclic phosphorylation takes place. Then electron transfer from FeS_x to cytochrome b_6 (cyt b_6) takes place, ensuring that the PS I RC is reduced.

energy output. The internal membrane also has folds, known as the chloroplast envelope, which contains a liquid, the stroma, and stacks of inner membrane discs or thylakoids (see Fig. 5). Stacks of these thylakoids are called grana. All pigment protein complexes needed for the light dependent reactions of photosynthesis are located in the thylakoid membranes. The dark reactions of photosynthesis occur in the stroma (see Fig. 5B).

Understanding the complex, multiphasic process of photosynthesis has many important scientific implications. From a biological perspective, understanding photosynthesis and how it varies among different organisms is important from structural biological, biochemical, evolutionary, and genetic standpoints. From a more physical perspective, understanding the physics of photosynthesis, especially the early events of light-harvesting EET and electron transfer, is extremely important as a model for solar cell science and technology [8-10]. Information gleaned could have practical applications for third or fourth generation photovoltaic devices, in either creating solar cells that mimic photosynthesis [11, 12] or actually using photosynthetic complexes in bioengineered devices [13, 14].

1.2 Photosynthetic Complexes

While the exact photosynthetic process can vary greatly in different types of organisms, the early events of photosynthesis are very similar for all organisms. The basic schematic for all is, as stated before, energy collection by light harvesting complexes and transfer to the RC for charge separation. Light harvesting and RC complexes are pigment-protein structures where the chlorophyll or other pigments are coupled to a protein structure, giving these complexes unique structures and pigment arrangements. Together the light harvesting and RC complexes make up the

photosynthetic unit (PSU) [1, 15]. The PSU is the building block for photophysical and photochemical processes in photosynthesis for an organism. By definition, in one PSU, one absorbed photon can yield a charge separated state in a reaction center. In order to increase the surface area for absorption, hundreds of light harvesting complexes per reaction center makes up a PSU (see Fig. 6). Different organisms may have different light harvesting complexes and reaction center complexes, but they all conform to this basic architecture of the PSU.

Though different photosynthetic light harvesting and RC complexes serve the same function, they each have their own highly specific and unique properties. For example, the PS I RC of cyanobacteria and green plants, has states lower in energy than the primary electron donor and these states can act as long wavelength antennas or as energy traps for photoprotection [16, 17]. The PS II RC of cyanobacteria and green plants is the only RC complex with a primary electron donor high enough in redox potential to oxidize water (1.1 V) [18].

Light harvesting complexes show highly unique properties as well. The light harvesting 2 (LH2) complex of purple bacteria has two highly symmetric chlorophyll rings, where one ring is strongly coupled resulting in a manifold of excitonic states (B850) while the other ring (B800) has weak coupling between chlorophyll dimers resulting in localized excitonic states [19, 20]. The CP43 light harvesting complex of cyanobacteria and plants has two quasi-degenerate states at 682.9 nm (B state) and 683.3 nm (A state), where the B state serves most likely as the main energy transfer pathway to the RC due to high correlation with higher lying energy states while the A state functions as more of an energy sink, with an excited state lifetime approaching the radiative limit

for a Chl transition (8 ± 1 ns) [21]. So while different light harvesting and RC complexes share the same basic purpose, each particular complex has their own specific niche and functionality for EET and/or electron transfer.

Since light harvesting complexes and reaction center complexes have distinct functional differences, and since the study of light harvesting and RC complexes has somewhat developed along independent paths, separate sections will be presented to discuss the highlights of important structural and spectroscopic research developments. Sections 1.2.1 and 1.2.2 will give an overview of historical and recent contributions from X-ray crystallography and ultrafast photon-echo, and hole-burning spectroscopy experiments for light harvesting and RC complexes, respectively. However, a more thorough treatment will be given to Section 1.2.2, especially regarding the PS I and PS II RCs, due to the fact that the research contained in this dissertation focuses on the EET and electron transfer properties of these RC complexes.

1.2.1 Light Harvesting Complexes

Light harvesting antenna complexes can be broadly separated into two classes: integral membrane antenna complexes and peripheral antenna complexes [2]. Integral membrane antennas are complexes in which the pigment-protein crosses the lipid bilayer. Peripheral antennas are complexes where the protein does not cross the lipid bilayer but coordinate with the pigment-protein complexes in the membrane. Peripheral antenna complexes function to transfer energy to the integral membrane complexes, where energy eventually travels to the reaction center. Peripheral antenna complexes include the phycobilisomes of cyanobacteria and red algae and the chlorosomes and Fenna-Matthews-Olsen (FMO) complex of green bacteria [2]. Due to the availability of a high

for *Rs. Molischianum* [27] and *Rds. Acidophila* [28], respectively. The structure of LH1 has been correlated to LH2 through electron density mapping by Ghosh et al. [29]; it is now thought that LH1 is a 16 fold symmetric ring that encloses the bacterial RC [30]. This structural data has stimulated much interest in the energy transfer properties of these complexes and the correlation with their cyclic structures. Theoretical investigations have modeled energy transfer in these rings through incoherent Förster hopping and exciton dynamics (see Chapter 2). Additional motivation for research on LH2 and LH1 is that the anoxygenic bacterial photosynthetic machinery is less complicated than the photosynthetic systems of oxygenic bacteria and plants, thus offering well-defined systems for studying EET and electron transfer processes. For those more interested, the spectral and energy transfer properties of LH2 and LH1 are summarized in references [19, 31, 32].

LHCII of PS II has had structural data available for many years, which has stimulated research into the properties of this complex. In 1994, Kühlbrandt et al. [33], through electron diffraction and electron microscopy experiments on two-dimensional crystals of LHCII at cryogenic temperatures, determined the structure of the trimeric form at 3.4 Å resolution (parallel to the crystal plane) and 4.4-4.9 Å (perpendicular to the crystal plane). Trimeric LHCII consists of three transmembrane α-helices and a short amphiphilic helix. Each monomer binds 12 Chls and 3 xanthophylls (Xan). The determination of this structure has been very important due to its high level of sequence homology with the minor light harvesting complexes of PS II complexes such as CP26/CP29 and LHCI of PS I [34]. Until recently [35], the structural determination did not provide a high enough resolution to correctly assign the positions of all the Chls and

14 and 16 Chls, respectively, and that for both CP43 and CP47, the Chls are arranged in layers on the stromal and luminal sides of the membrane except for one Chl equidistant between the membrane surfaces, forming stacks of Chls that span the membrane. Other earlier studies have suggested that CP43 and CP47 bind between 14-16 Chls [48, 50-52].

Many experimental investigations have been performed to determine the CP43/CP47-RC energy transfer kinetics. Frequency domain spectroscopic investigations (fluorescence line-narrowing [53] and hole-burning (HB) [48, 53, 54]) on isolated CP43/CP47 has shown the presence of a long lived energy trap (~ 50 ps) at 690 nm for CP47, which likely correlates to the lowest state of an excitonically coupled Chl dimer [53], while CP43 possesses two quasi-degenerate traps at ~ 683 nm that have dephasing times on the order of nanoseconds [48]. For comparison, ultrafast experiments for CP43/CP47 have shown energy transfer components of 200-400 fs and 2-3 ps [55]. Experiments on "core" PS II RC complexes also show similar results for frequency and time domain techniques, with HB experiments predicting CP43/CP47 to RC energy transfer times of 70-270 ps [44], and time-resolved fluorescence experiments predicting CP43/CP47 to RC energy transfer times of 1.5-10 ps [55]. Recent attention has also turned to the study of energy transfer in PS I-IsiA supercomplexes of cyanobacteria that form under iron stress conditions, where the IsiA complex is sequentially homologous to CP43 of PS II and is often referred to as CP43′ [56]. Preliminary experiments have shown that the spectral properties of CP43′ are very similar to CP43, but with a noticeable difference in that CP43′ possesses only one absorption band at ~ 682 nm and not two quasi-degenerate states like CP43 (see Chapter 5 for details).

bacterial X-ray structure was the four-subunit complex (LMHC) of *Rhodopseduomonas (Rps.) viridis* by Michel, Deisenhofer, and Huber [63-65]. Later, other groups determined the X-ray structure of the three-subunit complex (LMH) of *Rb. Sphaeroides* [66, 67].

Purple bacterial reaction centers can consist of either three or four protein subunits, depending upon the species [2]. The subunits are designated as light (L), medium (M), heavy (H), and/or cytochrome (C) [2, 69]. It should be noted, though, that these designations were made before the true molecular masses of the subunits could accurately be determined and do not indicate the true masses of the subunits (H is the lowest mass, L is the next heavier, and M is the heaviest mass). The reaction centers also contain a number of non-covalently bound cofactors, such as four bacteriochlorophyll molecules (BChl) – the bacteriochlorophyll special pair dimer (P_A, P_B) and the two accessory bacteriochlorophylls (B_A, B_B), two bacteriopheophytin molecules (BPh_A, BPh_B), two quinones (Q_A, Q_B), one metal atom (i.e. Fe 2^+), and usually one carotenoid [2]. The special pair BChls are interesting in that they are a strongly excitonically coupled dimer (~ 1350 cm^{-1} excitonic splitting at 4 K for *Rb. Sphaeroides* [70]), due to the small interplanar distance between these chlorins (see Fig. 8b), and also because they are the primary electron donor for electron transfer. The special pair BChls are referred to as P870 in *Rb. Sphaeroides* and P960 in *Rps. Viridis*. The above assignment is based on the maximum absorbance wavelength of their lowest excitonic bands, which for *Rb. Sphaeroides* and *Rps. Viridis* is at 870 and 960 nm, respectively.

In *Rb. Sphaeroides*, the L and M subunits are the core membrane structure, where both subunits consist of five transmembrane helices that are arranged in a pseudo-C2

symmetry. The H subunit is oriented on the cytoplasmic side of the intracytoplasmic membrane. The C subunit is not present in all purple bacterial reaction centers and is not considered an integral membrane protein since it does not posses any transmembrane segments [2]. The C subunits main function is to bind four heme molecules that can accept an electron from cyt c_2 to reduce the oxidized reaction center. Additionally, the non-covalently bound cofactors are also arranged in a pseudo-C2 symmetry. The special pair bacteriochlorophylls (P_A, P_B) are oriented to the periplasmic side of the membrane and are surrounded by B_A and B_B. The two bacteriopheophytins (BPh_A, BPh_B) are each located behind the corresponding bacteriochlorophylls (B_A, B_B), towards the cytoplasmic side. Correspondingly, the quinones are located behind the bacteriopheophytins. Overall, this orientation of cofactors forms two electron transfer chains or pathways for charge separation in the RC (see Fig. 7A).

Upon optical excitation, P870 forms P870* in *Rb. Sphaeroides*, and initial electron transfer occurs within a few picoseconds [71], forming $P_A H_A^-$ through $P_A B_A^-$. After approximately 200 ps, further electron transfer forms $P_A Q_A^-$ and then eventually $P_A Q_B^-$. In wild-type RCs, electron transfer always occurs along the A branch and minimally along the B branch [65, 66]. It is theorized that A-side electron transfer occurs preferentially due to the relative free energy difference between the initial excited state P870* and $P_A B_A^-$, with electron transfer along this side conserving more energy for proton pumping [71]. This overall electron transfer reaction that forms the stable charge-separated state is shown in Fig. 3. Interestingly, the recombination rates of the electron transfer (back to the primary electron donor) are ~ 50 times slower than the forward transfer rates [2]. These advantageous kinetics help allow for charge separation to have

monomeric form. Since most of these Chls and cofactors and part of the integral membrane antenna complex of PS I, they cannot be separated from the RC cofactors where charge separation occurs. PS I also occurs in a trimeric form in cyanobacteria, where the complex contains three RCs and ~ 270 antenna Chl molecules arranged in a C3-like symmetry.

The X-ray structure of trimeric cyanobacterial PS I from *Thermosynechococcus elongatus* is currently available at a resolution of 2.5 Å, determined by Fromme et al. [78]. Each monomer of the trimer is composed of 12 different protein subunits that bind 96 Chls, 22 carotenoids, three 4Fe4S clusters, 2 phylloquinones, and 4 lipids. The PSaA and PsaB subunits in the center of the monomer are the most important as they bind the RC Chls and cofactors along with the majority of the antenna pigments. The reaction center of PS I consists of six Chls (P700 special pair Chls, two A Chls, and two A_0 Chls), two phylloquinones (two A_1), and three iron sulfur (4Fe4S) centers, F_X, F_A, and F_B.

These cofactors are arranged in two symmetrical branches, like the bacterial RC, with pseudo-C2 symmetry. The P700 special pair are located most luminally compared to the other cofactors and are strongly coupled, like the bacterial RC, and form the primary electron donor P700* when optically excited. In fact, the P700 special pair is ~ 1-2 Å closer together than the bacterial special pair (6.3 Å vs. 7.5 Å); however, the coupling in P700 is not as strong due to less favorable orientation of the Chl transition dipole moments. The two symmetrical branches are labeled A and B, and contain the other A, A_0, and A_1 cofactors. The symmetry is then broken by the F_X iron sulfur center, which is located between the two branches. The $F_{A,B}$ clusters, which are not bound by PsaA or PsaB but rather PsaC, are located behind the F_X cluster. Fig. 8 shows the

the arrangement of various cofactors in the PS I reaction center.

The 90 antenna Chls surround the RC in each monomer in order to maximize the cross-sectional area available for light absorption. Except for two Chls, the minimum distance from any of the antenna Chls to the RC cofactors is ~ 20 Å. These two other Chls are ~ 14 Å from the RC cofactors and have been referred to as "linker" Chls, since it has been suggested that they function as 'connectors' for energy transport between the antenna and RC pigments [78, 79]. While cyanobacteria lack the LHCI complex present in PS I of green plants, there is high sequence homology between bacterial and plant PS I along with similar spectroscopic properties [80]. This indicates significant structural correlation between the two complexes. As a result, cyanobacterial PS I is often used as a structural model for plant PS I.

In cyanobacterial PS I, there is some discrepancy about the initial charge separation kinetics resulting from excitation of P700. For example, in references [81-83] it has been proposed that initial charge separation occurs in ~ 1 ps after P700 excitation; however, other researchers suggest that there is an additional slower phase of 6-10 ps due to energy equilibration among the RC cofactors [84, 85]. In primary charge separation, the A_0 Chl is thought to be the first electron acceptor that can be resolved spectroscopically, forming the $P700^+ A_0^-$ radical pair. The transfer times for the subsequent electron transfer reactions are more agreed upon, with the $P700^+ A_1^-$ radical pair forming in ~ 15-30 ps [82, 83, 85] and then $P700^+ Fe_X^-$ forming biphasically with time constants of ~ 25 and ~ 250 ns [86, 87]. Electron transfer is thought to be asymmetric in PS I, with transfer taking place on the A branch, as revealed recently by

6803 and *Thermosynechococcus elongatus* possess two and three red states, respectively [78], with the most convincing evidence for these conclusions being supplied by Small and coworkers through high-resolution HB experiments [16, 94, 95]. Through coupling high pressure and electric field to HB measurements, they found that different linear-pressure shift rates, magnitude of permanent dipole moment change ($f\Delta\mu$), and electron-phonon coupling strengths for spectral holes burned between 700-725 nm identified three low energy states that absorb at 708 (C708), 715 (C715), and 719 nm (C719) in *Thermosynechococcus elongatus* [16]. In *Synechocystis* PCC 6803, Small and coworkers identified only two low energy red states that absorb at 708 (C708) and 714 nm (C714) [94, 95]. For green plants it has been suggested that there are two red states absorbing at 706 and 714 nm [94, 95]. Additionally, there is discrepancy over the function of these red state pigments. Some have argued that they increase the light absorption area of the antenna, especially for oceanic cyanobacteria where shorter wavelengths of light are filtered out [96, 97, 98]. Others suggest that they act as reservoirs which funnel energy back to the RC to decrease back-transfer to the bulk antenna pigments where radiationless decay can occur, increasing the efficiency of the light harvesting process [78] or that they help to maintain optimal energy equilibration within the antenna [98].

Currently, most research on PS I involves the determination of the exact structural nature and assignment of the red state pigments. The location of at least some of the red states had been linked to the trimerization region in *Synechocystis* PCC 6803, as mutants that lacked the PsaL and PsaM protein subunits, which are responsible for the formation of trimers, show ~ 30% less red state absorption at C708 when compared to PS I trimers [95]. Mutants that lacked the Psa F or Psa K subunits, located at the opposite side of the

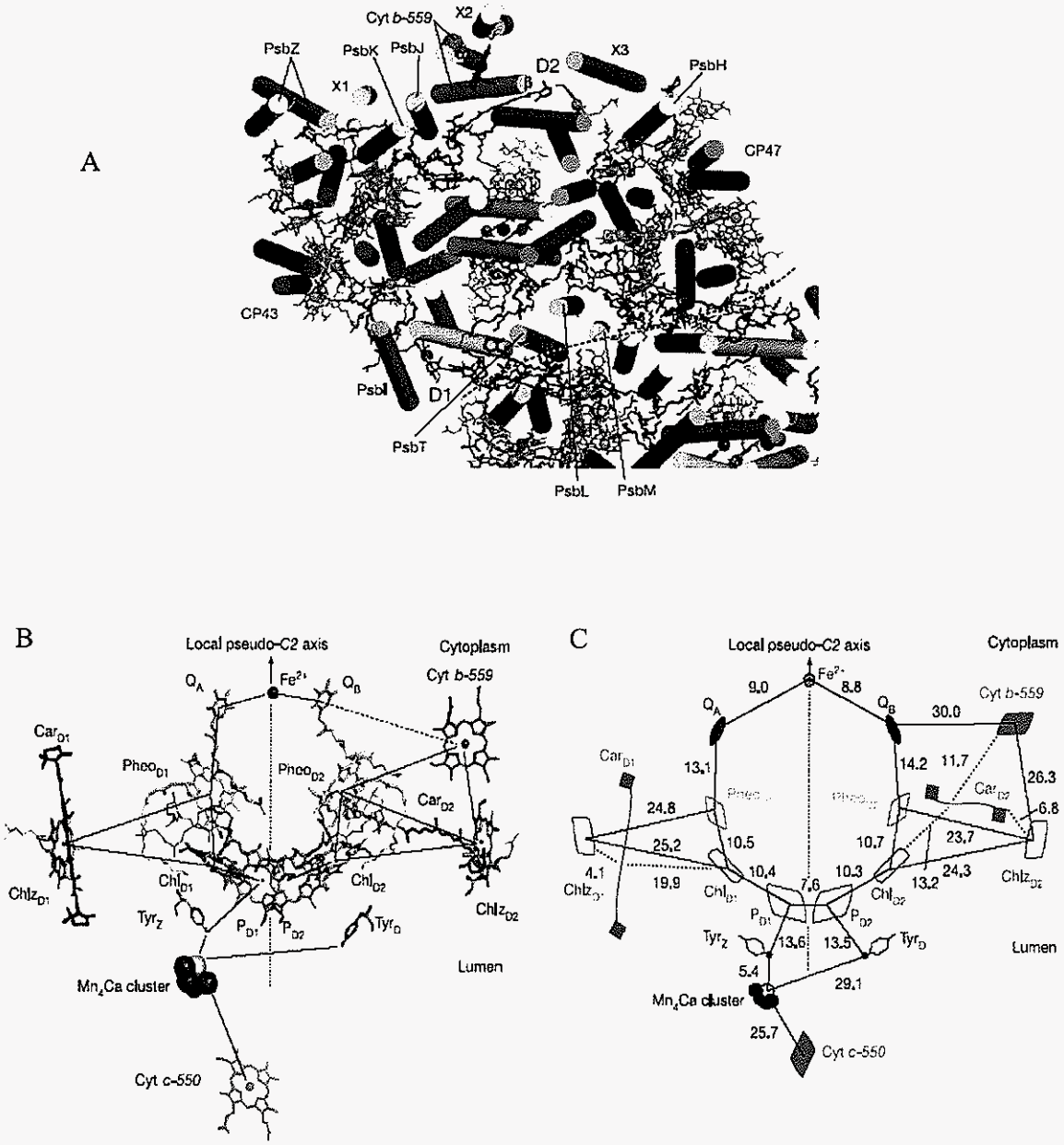

Figure 9. PS II X-ray structure at 2.5 Å resolution from Zouni et al. [108]. In (A), the PS II monomer from the cytoplasmic side is shown. The D_1, D_2 proteins are respectively colored yellow and orange, the CP43 and CP47 antenna complexes are purple and red, while a and b of cyt b_{559} are colored green and cyan. In (B), the structure and orientation of the RC cofactors is shown, while in (C) the respective distances (in Å) between the cofactors are shown. P_{D1}, P_{D2} are the P_1, P_2 Chls which are analogous the bacterial special pair (P_A, P_B) Chls. The labeling convention for the other cofactors follows correspondingly.

this, Durrant et al. [109] have proposed a "multimer" model for energy and electron transfer within the PS II RC. In this model, the RC pigments (P_1, P_2, Chl_1, Chl_2, $Pheo_1$, $Pheo_2$) are excitonically coupled in the dipole-dipole approximation; however, the inhomogeneous broadening of the individual Q_y states is comparable (~ 210 cm^{-1}) to these couplings, due to intrinsic structural disorder. This results in P680* being heterogeneous and not well defined. The multimer model predicts a similar intensity distribution of the Q_y states when compared to experimental spectra, with the two lowest states absorbing between 680-684 nm and the other states between 665-676 nm. However, there are some flaws with the multimer model. For example, the multimer model predicts that the reduction or oxidation of any cofactor should result in strong bleaching in the 680-684 nm region, due to the fact that there is significant contribution from all the cofactors to the lowest state [110].

Jankowiak et al. found, though, that in experiments on PS II RC-5 samples (see below) reduced by sodium dithionite, no prominent bleach at ~ 680 nm was seen. Instead, there was a resulting decrease in absorption at 668 nm, which was assigned to a Q_y state localized on $Pheo_2$ [111]. This reduction step was confirmed to be selective for $Pheo_2$ based on an additional $Pheo_2$ Q_x bleach (at ~ 544 nm) from the dithionite exposure [112] and that $Pheo_1$ can only be reduced by white light illumination and dithionite exposure [113]. In fact, reduction with dithonite and white light illumination by Jankowiak et al. on RC-5 samples showed a prominent bleach at ~ 680 nm, indicating that $Pheo_1$ is excitonically coupled to the other RC cofactors [112]. Jankowiak concluded then that $Pheo_2$ was excitonically decoupled from the other RC cofactors through dielectric screening caused by the local surrounding protein environment (e.g. an acidic

ultrafast vibrational spectroscopy experiments, that the triplet state is localized on Chl_1 [114]. They also argue that the since the triplet state is localized on Chl_1, it is most likely the primary donor state (P680*). However, they do not recognize the prediction of this phenomenon by the pentamer model, which also predicts that even though the triplet is localized on Chl_1, the primary donor composition is still heterogeneous and not localized on any particular cofactor.

The delocalization of the primary donor state predicted by the pentamer and multimer models has very important implications regarding the primary charge separation kinetics of PS II. Numerous groups have reported conflicting primary charge separation rates for both room temperature, (i.e. (0.4 ps^{-1}) [113, 1115], (3 ps^{-1}) [116-118], (8 ps^{-1}) [119], (21 ps^{-1}) [120]), and low temperature, (i.e. (~ 2-5 ps^{-1}) [121-126]), experiments. In addition, Prokhorenko and Holzwarth have reported low temperature (1.3 K) photon echo experiments in which theoretical modeling of the experimental spectra imply that the primary charge separation kinetics are highly dispersive (~ 2 ps-2 ns) and not single exponential [127]. Recently, HB experiments and theoretical simulations published by our group (see Chapter 4) have given further support to the heterogeneous nature of P680* suggested by the multimer and pentamer models. This heterogeneity manifests as highly dispersive primary charge separation kinetics where the primary donor state has the highest probability of being localized on either the P_1, P_2, or Chl_1 pigments but with significant contribution from all other coupled RC pigment cofactors.

After charge separation, the primary radical pair ($P680^+ Pheo_1^-$) is formed, where $Pheo_1$ is assumed to be the electron acceptor due to its stronger coupling to the other RC pigments compared to $Pheo_2$ [110] and by analogy with the bacterial RC. Then the

methods have several protocols and have shown varying levels of purity [130, 131]. In "isolated" PS II RC complexes, some preparations lack one peripheral Chl (RC-5) while other preparations provide the intact RC with all six Chls (RC-6) [119, 132]. In isolated RC-5 preparations, there is a pronounced shoulder at 684 nm that absorbs lower than the main absorption band at 680 nm. The nature of this 684 state has been debated extensively [133]. The most current interpretations suggest that the 684 nm state is the lowest energy state of the primary donor (P684) that originates from intact RC complexes, with the P680 state being the lowest energy state of that originates from the primary donor (P680) of perturbed RC complexes. Therefore, it was concluded that it is the intrinsic structural heterogeneity of these PS II RC complexes that results in the formation of P684 (see Chapter 4). Supercore RC complexes have shown interesting spectroscopic properties when compared to isolated RC complexes. Krausz et al have reported that P680 is red shifted in supercore complexes, as illumination at 685-700 nm results in efficient charge separation. They also report that deep spectral holes with lifetimes of 40-300 ps can be burned in the P680 band at low temperatures (~ 4 K). They explain this phenomenon as a result of "slow" energy transfer from the core CP43/CP47 antenna complexes to the RC. This slow energy transfer mechanism is supported by their experiments on "core" PS II samples in which time-resolved and transient absorption multiexponential decay times at room temperature are ~ 2x longer in CP47-RC "core" complexes versus isolated RC complexes [44-46].

Currently, the exact nature of charge separation and energy transfer in the PS II RC still eludes researchers. A higher resolution (< 2.5 Å) X-ray structure for PS II is clearly needed for certain assignment of pigment distances and positions. However,

complex and PS I. In Chapter 6, bulk hole-burning spectroscopy experiments and single-molecule spectroscopy experiments of on single PS I complexes were performed to characterize the connectivity of energy transfer between different pools of red state antenna pigments in *Synechocystis* PCC 6803 and *Thermosynechococcus elongatus*. Lastly, Chapter 7 provides a short introduction of current and future research on PCs that is impacting the developing field of molecular electronics, while Chapter 8 presents preliminary data for using trimeric photosynthetic PS I RC complexes as a basis for the nanoscale molecular electronic architecture for these types of devices. As stated before, photosynthetic pigment-protein complexes serve as an ideal model for photovoltaic cells, which will be needed in the 21st century due to exhaustion of traditional fossil fuel sources. Considering that the earth receives about 5.2 x 10^{21} kJ/year [10] of solar energy, the development of higher efficiency photovoltaics would have an enormous impact for renewable energy technology.

11. Kodis, G., Liddell, P. A., de la Garza, L., Clausen, P. C., Lindsey, J. S., Moore, A. L., Moore, T. A.; Gust, D., *J. Phys. Chem. A.* **2002**, 106, p. 2036.

12. Gust, D., Moore, T. A., Moore, A. L., Kennis, J. T. M., *J. Phys. Chem. B.* **2004**, 108, p. 414.

13. Lee, J. W. Lee, E. Greenbaum, *Phys. Rev. Lett.* **1999**, 79, p. 3294.

14. R. Das, P. J. Kiley, M. Segal, J. Norville, A. A. Yu, L. Wang, S. A. Trammell, L. E. Reddick, R. Kumar, F. Stellacci, N. Lebedev, J. Schnur, B. D. Bruce, S. Zhang, M. Baldo, *Nano Lett.* **2004**, 4, p. 1079.

15. Mauzerall, D., Greenbaum, N.L., *Biochim. Biophys. Acta* **1989**, 974, p. 119.

16. Reinot, T., Zazubovich, W., Hayes, J. M. and Small, G. J. *J. Phys. Chem. B* **2001**, 105, p. 5083.

17. Gobets, B., van Grondelle, R., *Biochim. Biophys. Acta*, **2001**, 1507, p 80.

18. Barber, J., Archer, M.D., *J. Photochem. Photobiol. A* **2001**, 142, p. 97.

19. Sundstrom, V., Pullertis, T., van Grondelle, R., *J. Phys. Chem. B* **1999**, 103, p. 2327.

20. Wu, H.-M., Rätsep, M., Jankowiak, R., Codgell, R.J., Small, G.J., *J. Phys. Chem. B* **1997**, 101, p. 7641.

21. Jankowiak, R., Zazubovich, V., Ratsep, M., Matsuzaki, S., Alfonso, M., Picorel, R., Seibert, M., Small, G.J., *J. Phys. Chem. B* **2000**, 104, p. 11805.

22. Camara-Artigas, A., Blankenship, R.E., Allen, J. P., *Photosynth. Res.* **2003**, 75, p. 49.

23. Matsuzaki, S., Zazubovich, V., Rätsep, M., Hayes, J.M., Small, G.J., *J. Phys. Chem. B* **2000**, 104, p. 9564.

37. Pieper, J., Irrgang, K.-D., Rätsep, M., Jankowiak, R., Schroetter, Th., Voigt, J., Small, G.J., Renger, G., *J. Phys. Chem. A* **1999**, 103, p. 2422.

38. Green, B.R., Durnford, D.G., *Ann. Rev. Plant Physiol. Mol. Biol.* **1996**, 47, p. 685.

39. Durnford, D.G., Deane, J.A., Tan, S., McFadden, G.I., Gantt, E., Green, B.R., *J. Mol. Evol.* **1999**, 48, p. 59.

40. Melkozernov, A.N., Schmid, V.H.R., Schmidt, G.W., Blankenship. R.E., *J. Phys. Chem. B* **1998**, 102, p. 8183.

41. Melkozernov, A.N., Schmid, V.H.R., Lin, S., Paulsen, H., Blankenship, R.E., *J. Phys. Chem. B* **2002**, 106, p. 4313.

42. Novoderexhkin, V., Salverda, J.M., van Amerongen, H., van Grondelle, R., *J. Phys. Chem. B* **2003**, 107, p. 1893.

43. Linnanto, J., Martiskainen, J., Lehtovuori, V., Ihalainen, J., Kananavicius, R., Barbato, R., Korppi-Tommola, J., *Photosynth. Res.* **2006**, 87, p. 267.

44. Krausz, E., Hughes, J. L., Smith, P., Pace, R., Peterson Arskoeld, S., *Photochem. Photobiol. Sci.* **2005**, 4, p. 744.

45. Hughes, J. L., Prince, B. J., Krausz, E., Smith, P. J., Pace, R. J., Riesen, H., *J. Phys. Chem. B* **2004**, 108, p. 10428.

46. Smith, P. J., Peterson, S., Masters, V. M., Wydrzynski, T., Styring, S., Krausz, E.; Pace, R.J., *Biochemistry* **2002**, 41, p. 1981.

47. Ferreira, K.N., Iverson, T.M., Maghlaoui, K., Barber, J., Iwata, S., *Science* **2004**, 303, p. 1831.

48. Jankowiak, R., Zazubovich, V., Ratsep, M., Matsuzaki, S., Alfonso, M., Picorel, R., Seibert, M., Small, G.J., *J. Phys. Chem. B* **2000**, 104, p. 11805.

62. Wild, A., and Ball, R., *Photosynthetic Unit and Photosystems: History of Research and Current View (Relationship of Structure and Function)*; Backhuys: Leiden, The Netherlands, 1997.

63. Michel, H., *J. Mol. Biol.* **1982**, 158, p. 167.

64. Deisenhofer, J., Epp, O., Miki, K., Huber, R., Michel, H., *J. Mol. Biol.* **1984**, 180, p. 385.

65. Deisenhofer, J., Epp, O., Miki, K., Huber, R., Michel, H., *Nature* **1985**, 318, p. 618-624.

66. Allen, J.P., Feher, G., Yeates, T.O., Rees, D.C., Deisenhofer, J., Michel, H., Huber, R., *Proc. Natl. Acad. Sci.* **1986**, 83, p. 8589.

67. Chang, C.H., Tiede, D.M., Tang. J., Smith, U., Norris, J., Schiffer, M., *FEBS Lett.* **1986**, 205, p. 82.

68. Camara-Artigas, A., Brune, D., Allen, J.P., *Proc. Natl. Acad. Sci.* **2002**, 99, p. 11055.

69. Feher, G., *Photosynth. Res.* **1998**, 61, p. 1.

70. Johnson, S.G., Tang, D., Jankowiak, R., Hayes, J.M., Small, G.J., *J. Phys. Chem.* **1989**, 93, p. 5953.

71. Haffa, A.L.M., Lin. S., Katilius, E., Williams, J.C., Taguchi, A.K.W., Allen, J.P., Woodbury, N.W., *J. Phys. Chem. B* **2002**, 106, p. 7376.

72. Kirmaier, C., Holten, D., Parson, W.W., *Biochim. Biophys. Acta* **1985**, 810, p. 49.

73. Kirmaier, C., Holten, D., Parson, W.W., *Biochim. Biophys. Acta* **1985**, 810, p. 33.

74. Martin, J.-L., Breton, J., Hoff, A.J., Migus, A., Antonetti, A., *Proc. Natl. Acad. Sci.* **1986**, 83, p. 957.

88. Xu, W., Chitnis, P.R., Valieva, A., van der Est, A., Brettel, K, Guergova-Kuras, M., Pushkar, Y.N., Zech, S.G., Stehlik, D., Shen, G., Zybailov, B., Golbeck, J.H., *J. Biol. Chem.* **2003**, 278, p. 27876.

89. Gibasiewicz, K., Ramesh, V.M., Lin, S., Woodbury, N.W., Webber, A.N., *J. Phys. Chem. B* **2002**, 106, p. 6322.

90. Gobets, B., van Stokkum, I.H.M., van Mourik, F., Dekker, J.P., van Grondelle, R., *Biophys. J.* **2003**, 85, p. 3883.

91. Damjanovic, A., Vaswani, H.M., Fromme, P., Fleming, G.R., *J. Phys. Chem. B* **2002**, 106, p. 10251.

92. Byrdin, M., Jordan, P., Krauss, N., Fromme, P., Stehlik, D., Schlodder, E., *Biophys. J.* **2002**, 83, p. 433.

93. Bruggemann, B., Sznee, K., Novoderezhkin, V., van Grondelle, R., May, V., *J. Phys. Chem. B* **2004**, 108, p. 13536.

94. Hayes, J.M., Matsuzaki, S., Rätsep, M., Small, G.J., *J. Phys. Chem. B* **2000**, 104, p. 5625.

95. Rätsep, M., Johnson, T.W., Chitnis, P.R., Small, G.J., *J. Phys. Chem. B* **2000**, 104, p. 836.

96. Trissl, H.-W., *Photosynth. Res.* **1993**, 35, p. 247.

97. Trissl, H.-W. and Wilhelm, C., *Trends Biochem. Sci.* **1993**, 18, p. 415.

98. Grotjohann, I. and Fromme, P., *Photosynth. Res.* **2005**, 85, p. 51.

99. Satoh, S. and Tanaka, A., *FEBS Lett.* **2002**, 528, p. 235.

100. Trebst, A.Z., *Naturforsch* **1985**, 41, p. 20.

101. Sayre, R.T., Anderson, B., Bogorad, L., *Cell* **1986**, 47, p. 601.

115. Wasielewski, M.R., Johnson, D.G., Seibert, M., Govindjee, R., *Proc. Natl. Acad. Sci. U.S.A.* **1989**, 86, p. 524.

116. Wiederrecht, G.P., Seibert, M., Govindjee, R., Wasielewski, M.R., *Proc. Natl. Acad. Sci. U.S.A.* **1994**, 91, p. 8999.

117. Schelvis, J.P.M., van Noort, P.I., Aartsma, T.J., van Gorkom, H.J., *Biochim. Biophys. Acta* **1994**, 1184, p. 242.

118. Gatzen, G., Müller, M.G., Griebenow, K., Holzwarth, A.R., *J. Phys. Chem.* **1996**, 100, p. 7269.

119. Greenfield, S.R., Seibert, M., Govindjee, Wasielewski, M.R., *J. Phys. Chem. B* **1997**, 101, p. 2251.

120. Merry, S.A., Kamzaki, S., Tachibana, Y., Joseph, D.M., Porter, G., Yoshohara, K., Barber, J., Durrant, J.R., Klug, D.R., *J. Phys. Chem. B* **1996**, 100, p. 10469.

121. Jankowiak, R., Tang, D., Small, G. J., Seibert, M., *J. Phys. Chem.* **1989**, 93, p. 1649.

122. Tang, D., Jankowiak, R., Seibert, M., Small, G. J., *Photosynth. Res.* **1991**, 27, p. 19.

123. Wasielewski, M. R., Johnson, D., Govindjee, Preston, C., Seibert, M., *Photosynth. Res.* **1989**, 22, p. 89.

124. Visser, H. M., Groot, M.-L., van Mourik, F., van Stokkum, I. H., Dekker, J. P., van Grondelle, R., *J. Phys. Chem.* **1995**, 99, p. 15304.

125. Greenfield, S. R., Seibert, M., Wasielewski, M. R., *J. Phys. Chem. B* **1999**, 103, p. 8364.

CHAPTER 2 – ENERGY TRANSFER IN PHOTOSYNTHETIC COMPLEXES

2.1 Introduction

Probably the most unique physical aspects of photosynthetic complexes (PCs) are their complex, inter-connected energy transfer processes. These arise from the special arrangements and couplings of different photosynthetic pigment molecules to account for specific events during energy collection and eventual charge separation; resulting in a wide variation of energy transfer channels, rates, and yields [1-7]. Consequently, energy transfer in PCs has been modeled through many different approximations. For example, energy transfer has been modeled as localized Förster donor - acceptor states [8] in the weakly coupled B800 dimer ring of purple bacterial LH2 [1, 2]. Energy transfer has also been modeled through exciton formation [10], as in the PS II reaction center (RC) [6, 34], and through coherent excitonic relaxation in strongly coupled antenna systems, such the Fenna-Matthews-Olsen (FMO) light harvesting antenna complex [7].

Thus, it is important to understand the physical picture of EET for photosynthetic systems, which can be described in terms of two limiting cases: weak and strong coupling between donor and acceptor molecules (states) [11, 12]. In the weak coupling limit, energy transfer can be thought of as hopping process between independent, localized states. In the strong coupling limit, the electronic states cannot be thought of as localized on individual molecules, as new intermolecular coherent eigenstates (excitonic states, see Section 2.4) are formed by virtue of strong electronic coupling, and EET is thought of as a perturbation induced relaxation process between these coherent excitonic states.

acceptor absorption, normalized to unit area on an energy scale [8]. Also, it is assumed that the electronic transition moment does not change upon molecular nuclear motions and that the thermalization of molecular vibrations and bath phonons occur on a time scale much faster than energy transfer.

In Förster theory, dipole-dipole coupling can safely be assumed when the electronic transitions of D and A are weakly coupled and the distance between them is greater than the size of the molecules, i.e. there is no wavefunction overlap [8, 15]. Usually this corresponds to a separation distance between the donor-acceptor of ~ 1-10 nm. If these requirements are met, higher order multipole terms along with antisymmetrization (electron exchange) terms can be neglected and the electronic coupling matrix element between D and A, in Eq. 2.1 is

$$\langle D^* A | V_{DA} | DA^* \rangle \equiv V_{DA} = \frac{\kappa \left| \vec{\mu}_D \right\| \vec{\mu}_A \right|}{R_{DA}^{\ 3}} \tag{2.2}$$

where $\vec{\mu}_D$ and $\vec{\mu}_A$ are the electronic transition dipole moment vectors of D and A, respectively. V_{DA} is dependent only on the electronic wavefunctions since the Born-Oppenheimer approximation is invoked during the derivation of Eq. 2.1. R_{DA} is the distance between the center of D and the center of A in angstroms. κ is the orientation factor and is defined as: $\kappa \equiv \hat{\mu}_D \cdot \hat{\mu}_A - 3(\hat{\mu}_D \cdot \hat{\mathrm{R}}_{DA})(\hat{\mathrm{R}}_{DA} \cdot \hat{\mu}_A)$ where the circumflex symbol (^) represents the unit vector of the corresponding vector. Depending on the orientation, κ can range in value from –2 to 2 (see Fig. 1). As shown in Fig. 1, κ^2 is largest, and the transfer rate is enhanced, when $\vec{\mu}_D$ and $\vec{\mu}_A$ is in either a head-to-head or

head-to-tail orientation. For molecules with random orientations of dipole vectors, κ = 2/3 [16].

The spectral overlap, $J(\nu)$, term in Eq. 2.1 is another result of invoking the Born-Oppenheimer approximation. In the Born-Oppenheimer approximation [17], separation of the electronic and vibrational wavefunctions is allowed as the nuclear motions of the atoms are assumed to be on a much slower timescale compared to the motions of the electrons during the optical excitation of either D or A. Therefore, the vibrational transitions of D and A are expressed in $J(\nu) = \varepsilon_A(\nu) \cdot F_D(\nu) \cdot 1/\nu^4$, where $\varepsilon(\nu)$ is the molar decadic extinction coefficient of A in L/(mol·cm), $F_D(\nu)$ is the normalized emission spectrum of D, and ν is the wavenumber in cm^{-1}. $\varepsilon_A(\nu)$ and $F_D(\nu)$ are expressed as

$$\varepsilon_A(\nu) = \frac{8\pi^3 N' \nu}{3hcn\ln(10)} \mu_A^2(\nu) \tag{2.3}$$

and

$$F_D(\nu) = \frac{64\pi^3 n \nu^3 \tau}{3h} \mu_D^2(\nu) \tag{2.4}$$

where N' is Avogadro's constant divided by 1000, h is Planck's constant, c is the speed of light in vacuum and units of cm^2/s, n is the refractive index of the solvent, and τ is the total dephasing time of D (for the definition of pure dephasing time, see Chapter 3, Sect 3.1). $\mu_D^2(\nu)$ and $\mu_A^2(\nu)$ are the vibronic transition dipole moments averaged over all thermal and vibrational levels, respectively. Thus, $J(\nu)$ is referred to as the Franck-Condon factor weighted density of states [16, 18] (for a more detailed description of the

Franck-Condon principle, see Chapter 3, Sect. 3.1). The value of $J(\nu)$ can range from 0 to 1, with a value of 1 indicating perfect spectral overlap (see Fig. 2A).

With terms such as spectral overlap, donor fluorescence, and acceptor emission, one may think that energy transfer in Förster theory occurs radiatively, with D emitting a photon that is captured by A. This is incorrect; however, energy transfer in Förster theory is a quantum mechanical non-radiative process that occurs between two states that are resonant in energy [8, 15, 19]. This resonance condition is required by conservation of energy, so that the energy of the system is same after energy transfer as it was before, because of this Förster energy transfer is often referred to as Förster resonance energy transfer (FRET) [20]. For an illustration of the resonance condition, see Fig. 2B.

The Förster rate equation (Eq. 2.1) can also be recast [8, 21] in a slightly more elegant form

$$k_{DA} = \frac{1}{\tau}\left(\frac{R_0}{R}\right)^6, \tag{2.5}$$

where R is the distance between the centers of molecules D and A and R_0 is expressed as

$$R_0^6 \equiv \frac{9\ln(10)}{128\pi^5 n^4 N'}\kappa^2 \int d\nu * \frac{F_D(\nu)\varepsilon_A(\nu)}{\nu^4} \tag{2.6}$$

and is defined as the distance where energy transfer is 50% efficient. Eq 2.5 shows that the energy transfer rate is inversely proportional to the distance between D and A to the sixth power and that when $R_0 = R_{DA}$, the energy transfer rate is equal to the total dephasing time of D.

While Eqs. 2.1 and 2.5 are relatively straightforward, there are implications and limits with Förster theory that must be recognized. As mentioned previously, Förster theory assumes that phononic and vibrational relaxation, which is on the order of ~ 1 ps,

Lastly, since dipole-dipole coupling is only valid when the *D-A* distance is greater than the size of the molecules, closely spaced molecules cannot be modeled in this approximation. When the *D-A* distances are small enough for wavefunction overlap, electron exchange interactions must be taken into account for the electronic coupling (see Fig. 3). Electron exchange energy transfer occurs in strongly coupled pigment dimers and the primary electron donors of RC complexes. For example, primary charge separation in the bacterial RC has been modeled through a Marcus formalism via a Dexter coupled electron exchange reaction [23, 24]. However, primary electron transfer for other photosystems (i.e. PS I and PS II) is more sophisticated, and cannot be assumed to follow this approximation. Interestingly, higher order coulombic terms (e.g. monopole-monopole, dipole-quadrapole) can activate energy transfer between allowed-forbidden transitions; however, these transitions are only weakly allowed and usually only significant when the electronic coupling is considered to be stronger. This assumption of higher order electronic coupling terms to trigger energy transfer is referred to as Dexter theory [14] and models have been developed to account for these for energy transfer between photosynthetic pigment molecules [26-28].

2.4.1 Molecular Excitons

While Förster and Dexter type theories are good approximations for weakly coupled pigments, they start to lose their physical meaning for more strongly coupled systems where excitations cannot assume to be localized. Instead, excitons (coherent inter-molecular excited states) form in these photosynthetic systems [6, 7, 29]. Here, the basic physics of excitons are described, and then, in later sections, applied to energy transfer in photosynthetic pigment complexes.

In a periodic, ordered molecular system, such as a molecular aggregate, the excitation of a single molecule can be represented by

$$\left[\sum_{n} H_n + \sum_{n,m}{}' \frac{1}{2} V_{nm} - E_{ex}\right] |\varphi\rangle = 0 \tag{2.7}$$

where H_n designates the energy operator of the nth molecule and φ is the wavefunction of the system. V_{nm} is the interaction energy between the excited molecule and its nearest neighbor, second nearest neighbor, and so on; E_{ex} is the molecular excitation energy [10]. The system wavefunction, φ, is defined as the antisymmetrized product of the individual molecular wavefunctions

$$\varphi_{ex} = \varphi_n^{ex} \prod_{\substack{m \\ n \neq m}} \varphi_m^g \tag{2.8}$$

where φ_n^{ex} is the excited state wavefunction of the nth molecule and φ_m^g are the ground state wavefunctions of the other molecules in the aggregate [10].

When the interaction energy in Eq. 2.7 is large enough, the excitation is no longer localized on the αth molecule but is transferred to the other molecules in the crystal, spreading as an excitation wave, which travels as an electrostatically bound electron-hole pair that eventually recombines and annihilates. This collective excitation is referred to as an *exciton*. Excitons are defined between two limiting cases, where the electron-hole pair is either tightly bound (Frenkel exciton) or loosely bound (Mott-Wannier exciton) [10]. In Frenkel excitons, the excited electron is located on the same molecule or atom along with the hole. However, as the excitation travels as a wave through the crystal or ordered aggregate, the electron-hole pair "hops" from molecule to molecule (see Fig 4A). Frenkel excitons are the type of excitons that are discussed in this section, and usually

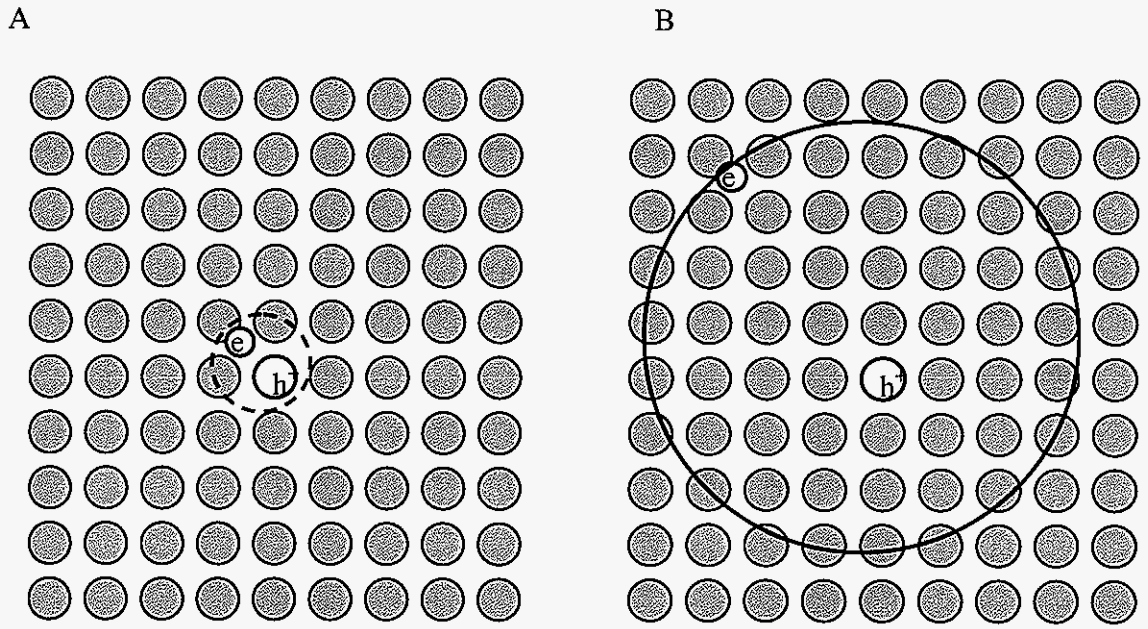

Figure 4. (A) Schematic of a Frenkel exciton. The electron (e^-) - hole (h^+) pair is tightly bound and as it travels through the molecular lattice, with an electron-hole separation distance less than the unit cell length. However, the excitation is considered a superposition of all the wavefunction in the lattice (Bloch form) and is thus considered to be delocalized over all the molecules in the lattice. (B) Schematic of a Mott Wannier exciton. The electron-hole pair is loosely bound, which results in electron-hole separation distances greater than the unit cell length. Mott-Wannier excitons are not observed in organic molecular systems due to their low dielectric constants. For Mott-Wannier excitons to form, a large dielectric constant is needed so that electron hole interaction is sufficiently weak to allow large electron hole separation distances [30].

A dimer in this sense refers to a pair of electrostatically interacting chlorophyll pigment molecules (either identical or non-identical) that are spatially separated, and not necessarily in van der Waals contact. For two identical molecules, though, the Hamiltonian due this interaction is

$$\left\langle \varphi_1^g \varphi_2^g \left| H_1 + H_2 + V \right| \varphi_1^g \varphi_2^g \right\rangle = E_g \tag{2.15}$$

where the ground state wavefunction of the dimer is taken to be a product of the molecular wavefunctions, as in molecular crystals:

$$\psi_g = \varphi_1^g \varphi_2^g \tag{2.16}$$

and the ground state energy of the dimer can be expressed as

$$E_g = \varepsilon_1^g + \varepsilon_2^g + D_g \tag{2.17}$$

Thus, the coupling between the two molecules shifts the ground state energy of the dimer by $D_g \equiv V_{00} \equiv \left\langle \varphi_1^g \varphi_2^g \left| V \right| \varphi_1^g \varphi_2^g \right\rangle$. D_g is often referred to as the *ground dispersion energy.*

The excited state wavefunction of the dimer can be represented as

$$\psi_{ex} = \frac{1}{\sqrt{2}} \left[\varphi_1^{ex} \varphi_2^g \pm \varphi_1^g \varphi_2^{ex} \right] \tag{2.18}$$

or more simply by

$$\psi_{ex} = \frac{1}{\sqrt{2}} \left[\psi_{ex}^1 \pm \psi_{ex}^2 \right] \tag{2.19}$$

$$\psi_{ex}^1 = \varphi_1^{ex} \varphi_2^g$$

$$\psi_{ex}^2 = \varphi_1^g \varphi_2^{ex}$$

where the wavefunction is both normalized and orthogonal.

condensed phase [16, 33]. The solvent shift usually causes a decrease in excitation energy, yielding a red shift of the excitonic absorption bands (see Fig 5).

Since the Coulomb coupling of V_{res} is usually considered in the dipole-dipole approximation, the relative orientation of the molecular transition dipole moment vectors in the dimer determines the oscillator strength and absorption intensity of each excitonic state. In the case where the dimer consists of two identical molecules, its transition dipole strength, I_{dim}, from the ground to the one quantum excited state, for each excitonic state, is [33]

$$I_{\dim}(\pm) = \left|\left\langle \psi_g \left| \mu_1 + \mu_2 \right| \psi_{ex} \right\rangle\right|^2 = I_{mol}(1 \pm \cos\theta) \tag{2.25}$$

where $\mu_{n=1,2}$ is the dipole moment operator of the respective molecules, I_{mol} is the molecular dipole strength, and θ is the angle between the molecular transition dipole moment vectors. The + and - labeling refers to the split excitonic states of the dimer (Eqs. 2.22.a and 2.22.b, respectively). For illustration, possible orientations of the transition dipole moment vectors in an excitonically coupled dimer of chlorophyll pigment molecules are diagrammed in Fig. 6, along with how these orientations determine the magnitude/sign of V_{res} and dipole (oscillator strength) of the excitonic bands.

In photosynthetic complexes, pigment molecules experience different local environments due to the surrounding protein matrix. Therefore, it cannot always be assumed that the site energies of pigment molecules will be the same. If a dimer is composed of two molecules with inequivalent excitation site energies of difference δ, then their energies can be "rezeroed" to δ/2 and -δ/2, respectively. The Hamiltonian

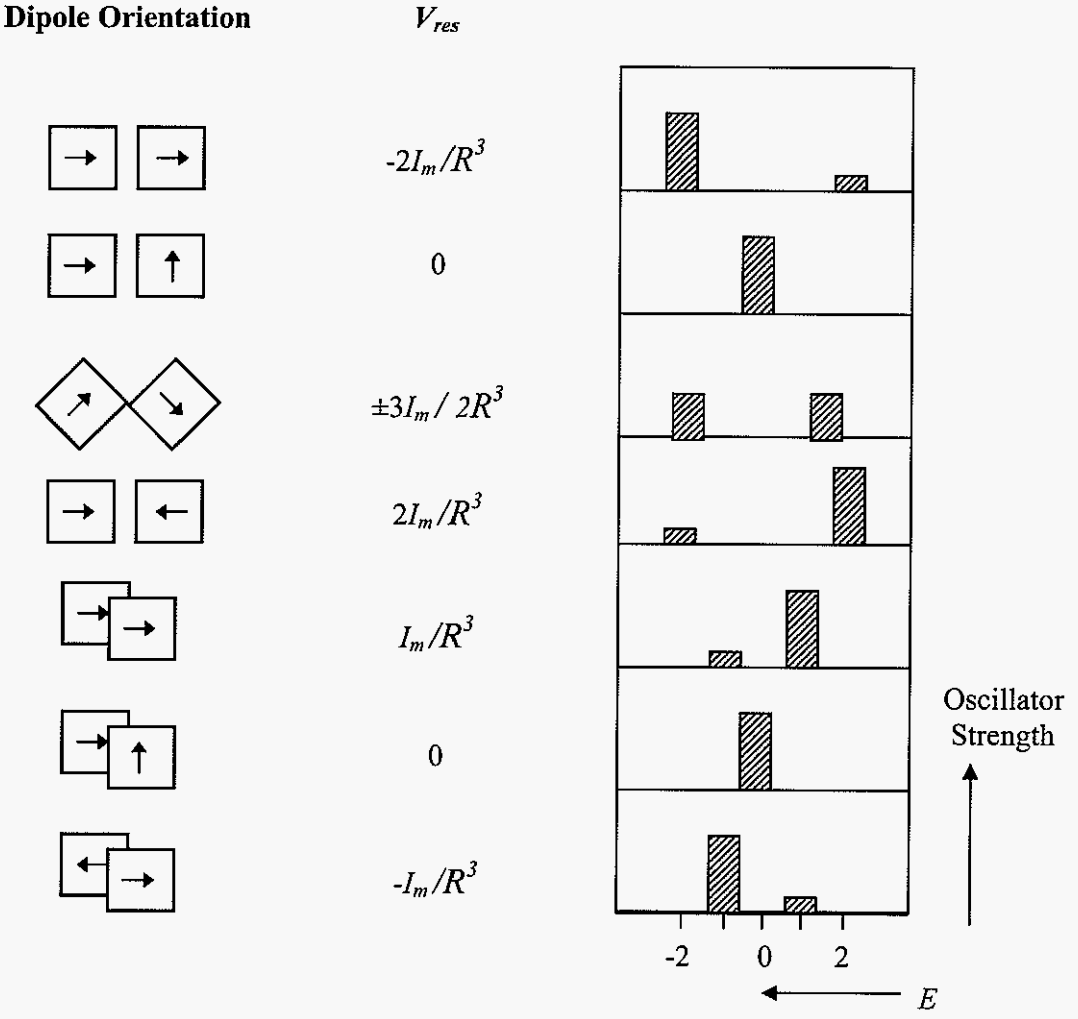

Figure 6. Schematic of excitonic band dipole orientations, oscillator strengths, and energies [34]. In the leftmost column, the orientation of the molecules and their dipole moments are shown. The squares represent molecular planes and the solid arrows, the transition dipole moment vectors. The excitonic coupling between the molecules is assumed to be dipole-dipole and is given by $V_{res} = V_{DA} \equiv \kappa I_m/R^3$ where $I_m = |\vec{\mu}_D \| \vec{\mu}_A|$ (see Eq. 2.2). The energy, E, (in units of I_m/R^3) and oscillator strength of the split excitonic bands are shown in the right most column.

In such aggregates, the excited state Hamiltonian is:

$$H = \sum_{n,m} \varepsilon_n^{ex} \delta_{nm} + \sum_{n,m}{}' V_{nm} \tag{2.28}$$

(where the excited state dispersion energies are discarded for simplicity) and the normalized excited state wavefunctions for the coupled chlorin molecules are

$$\varphi_{ex,n} = \sum_n \varphi_n^{ex} \prod_{\substack{m \\ n \neq m}} \varphi_m^g \tag{2.29}$$

By then taking the wavefunctions in Eq. 2.29 and expanding them about the Hamiltonian in Eq. 2.28 the following result is obtained

$$H = \sum_n \varepsilon_n^{ex} \left\langle \varphi_n^{ex} \middle| \varphi_n^{ex} \right\rangle + \sum_{n,m}{}' \left\langle \varphi_n^{ex} \middle| V_{nm} \middle| \varphi_m^{ex} \right\rangle \tag{2.30}$$

which shows that the Hamiltonian depends only on the excited state wavefunctions and energies. This expansion generates a $n \times n$ matrix and can be diagonalized to solve for the excitonic energies (E_α) and wavefunctions ($|\alpha\rangle$).

The excitonic wavefunctions are simply

$$|\alpha\rangle = \sum_n c_{\alpha n} \left| \varphi_n^{ex} \right\rangle \tag{2.31}$$

where the excited state molecular wavefunctions serve as a basis for the normalized and orthogonal excitonic wavefunctions, and the coefficients determine the contribution of each molecular wavefunction to the excitonic band. The coefficients can also be used to determine the excitonic transition dipoles

$$\hat{\boldsymbol{\mu}}_{\boldsymbol{\alpha}} = \sum_n c_{\alpha n} \hat{\mu}_n \ , \tag{2.32}$$

crystallography structures (≤ 1.6 Å) [39] are not available for most PCs [40-42]. Therefore, the precise positions of the chlorin molecules to calculate the electrostatic coupling are not available, and, more importantly, since the chlorin-chlorin distances are not adequately defined, what coupling approximation should be used, e.g. dipole-dipole, full Coulomb, etc.

2.4.4 Energy Transfer via Relaxation in Photosynthetic Excitons

As discussed previously, when $V/\Delta >> 1$ the Condon approximation breaks down and the treatment of individual photosynthetic pigments as localized donor and acceptor eigenstates that transfer energy through an incoherent hopping process is no longer valid. Instead, energy transfer occurs through coherence and relaxation of excitonic states. In this "exciton picture", the energy transfer can be calculated using a Fermi-Golden rule expression, like the Förster equation, that is derived from first-order perturbation theory. The perturbation in excitonic relaxation, however, is not the electronic coupling (V), as in Förster theory, but the electron-phonon coupling (dynamic disorder) [1, 25].

Since the Condon approximation is no longer valid, the electronic wavefunction coordinates are no longer independent of the vibrational wavefunction coordinates and the excitonic Hamiltonian must be modified. The electron-phonon perturbation can be expressed by partitioning the excitonic Hamiltonian into H_0, the zero order contribution (Eq. 2.28), and ΔH, the perturbation operator,

$$H^{ex} = H_0 + \Delta H \tag{2.34}$$

The perturbation operator, also referred to as the non-adiabaticity operator or Born-Oppenheimer correction term, takes into account the dependence of the electron-phonon interaction potential, V_{int}, for a fixed configuration of the phonon "promoting mode"

since $\left|\left\langle n_{\mathrm{p}}+1\left|b_{\mathrm{p}}+b_{\mathrm{p}}^{+}\right|n_{\mathrm{p}}\right\rangle\right|^{2}=\left\langle\tilde{n}_{\mathrm{p}}+1\right\rangle$, where $\left|n_{\mathrm{p}}, n_{\mathrm{p}}+1\right\rangle$ are the vibrational wavefunctions for the promoting mode(s) and $\tilde{n}_{\mathrm{p}}$ is the thermal occupation number, $\left[\exp(\hbar\omega_{\mathrm{p}}/kT)-1\right]^{-1}$ [45]. The spectral density in Eq 2.38 is reduced by ω_{p} due to one-phonon emission; if there is one-phonon absorption ($\left\langle\tilde{n}_{\mathrm{p}}\right\rangle$), the spectral density is increased by ω_{p} [16].

To determine explicit expressions for the exciton-phonon interaction (perturbation operator, ΔH) in Eq 2.41, the excitonic Hamiltonian (Eq. 2.28) is expanded in a Taylor series about the lattice coordinates $\{\mathbf{R}=0\}$, which the phonon coordinates, q_{p}, are dependent upon. In this expansion all the linear terms are collected, along with quadratic terms that describe harmonic phonons. This results in the following equation [10, 46]

$$H^{ex}(R)=H_0(R)+H_{PH}(R)+H_{EX-PH(1)}(R)+H_{EX-PH(2)}(R) \tag{2.39}$$

$H_0(R)$, the zero-order contribution (see above), determines the crude adiabatic energies for the exciton bands and is written as

$$H_0(R)=\sum_n\left[\varepsilon_n^{ex}+D_n^{ex}(R)\right]\,B_n^{+}B_n+\sum_{n,m}V_{nm}(R)\;B_n^{+}B_m\;, \tag{2.40}$$

where the excited state dispersion energies are included, in Eq. 2.40 $D_n^{ex}(R)=\sum_{m\neq n}D_{ex,nm}(R)$ and the expanded Hamiltonian is expressed in terms of ladder operators. $H_{PH}(R)$, the phonon Hamiltonian, is

$$H_{PH}(R)=\sum_{\mathbf{q}s}\hbar\omega_s(\mathbf{q})b_{\mathrm{q}}^{+}b_{\mathrm{q}}\;, \tag{2.41}$$

$$H_{EX-PH(2)}(R) = N^{-1/2}\sum_{\mathbf{k},qs} B^{+}(\mathbf{k})B(\mathbf{k})\chi_s(\mathbf{q})(b_{qs} + b^{+}_{-qs}) \ , \tag{2.47}$$

where

$$F_s(\mathbf{k},\mathbf{q}) = \sum_{j,m(\neq 0)} \alpha(s,\mathbf{q})e_s^j(\mathbf{q})\left[\left(\frac{\partial V_{0m}}{\partial R_0^j}\right)_0 + e^{i\mathbf{q}\cdot(\mathbf{m})}\left(\frac{\partial V_{0m}}{\partial R_m^j}\right)_0\right] e^{i\mathbf{k}\cdot(\mathbf{m})} \tag{2.48}$$

$$\chi_s(\mathbf{q}) = \sum_{j,m(\neq 0)} \alpha(s,\mathbf{q})e_s^j(\mathbf{q})\left[\left(\frac{\partial D_{0m}^{ex}}{\partial R_0^j}\right)_0 + e^{i\mathbf{q}\cdot(\mathbf{m})}\left(\frac{\partial D_{0m}^{ex}}{\partial R_m^j}\right)_0\right] \tag{2.49}$$

with $\alpha(s,\mathbf{q}) = \left(\hbar / 2\omega_s(\mathbf{q})I_j\right)^{-1/2}$. Eqs. 2.46 and 2.47 both assume that there is only one molecule per unit cell, and thus only one exciton branch. Thus, the final expression for energy transfer is obtained trivially by inserting these expressions into Eq. 2.38, which contain the delocalized excitonic and nuclear wavefunctions.

It is noted that Eqs. 2.46 and 2.47 imply two limiting cases for exciton-phonon scattering, when $H_{EX-PH(1)} >> H_{EX-PH(2)}$ and when $H_{EX-PH(1)} < H_{EX-PH(2)}$. If the former is the limiting case, the modulation of the V term is dominant, and the exciton-phonon coupling is considered to be weak and non-local. In this case, exciton scattering, and thus energy transfer, occurs from one **k**-value to another (see Fig. 7). If the latter is the limiting case, the modulation of the D term is dominant, and the exciton-phonon coupling is considered to be strong and local. In this case, exciton scattering occurs, but there is no change in **k**-value and energy transfer from one band to another does not occur. Instead, this modulation of the molecular energy D term shifts the equilibrium of the intermolecular coordinates, deforming the lattice around the excited molecule. If the electron-phonon coupling is strong enough, this deformation can localize or even trap the exciton. These *self-trapped excitons* should not be viewed as being "localized" in space

and time, but rather moving through the lattice at a slow velocity. Self-trapped excitons in photosynthetic complexes [48, 49] are analogous to *polarons* in molecular crystals [30].

Alternatively, exciton relaxation can also be modeled through a density matrix picture approach, which allows for a time-evolution description of the coherence of the excitonic matrix elements. Thus, the downward energy cascading between excitonic bands can be followed through time. This approach is specifically called Redfield relaxation theory [50, 51]. In Redfield theory, the density operator ρ is projected into a reduced Liouville space that describes the electronic excitation degrees of freedom but averages out the phonon degrees of freedom. A second-order expansion of the Hamiltonian is then performed to determine the exciton-phonon Hamiltonian, which reduces the density matrix equation to [1, 33]

$$\frac{d\rho_{nm}(t)}{dt} = \frac{-i}{\hbar}[H_0, \rho]_{nm} - \sum_{pq} \mathbf{R}_{nm,pq}\rho_{pq}(t) \tag{2.50}$$

where $\rho_{\alpha\beta}$ is the density matrix operator for states α and β, respectively. The first term on the R.H.S. in Eq. 2.50 details the coherence of the system, which depends on the zero-order Hamiltonian (see Eq 2.30), while the second term on the R.H.S. details the coherence loss due to the system-bath interaction described by the Redfield tensor $\mathbf{R}$. The Redfield tensor $\mathbf{R}_{nm,pq}$ is dependent on the electron-phonon coupling expressions from Eqs. 2.46-7 and connects all the density matrix elements. $\mathbf{R}_{nn,mm}$ is the rate constant for the population transfer from the m^{th} to the n^{th} state; $\mathbf{R}_{nm,nm}$ is the dephasing of the coherence between the m^{th} and n^{th} states; and $\mathbf{R}_{nm,pq}$ is the coherence transfer term between p and q states to n and m states.

References

1. Sundstrom, V., Pullertis, T., van Grondelle, R., *J. Phys. Chem. B* **1999,** 103, p. 232.
2. Hofmann, C., Ketelaars, M., Matsushita, M., Michel, H., Aartsma, T.J., Kohler, J., *Phys. Rev. Lett.* **2003**, 90, p. 013004/1.
3. Hayes, J.M., Matsuzaki, S., Ratsep, M., Small, G.J., *J. Phys. Chem B* **2000**, 104, p. 5625.
4. van Amerongen, H. and van Grondelle, R., *J. Phys. Chem. B* **2001**, 105, p. 604.
5. Jankowiak, R., Zazubovich, V., Ratsep, M., Matsuzaki, S., Alfonso, M., Picorel, R., Seibert, M., Small, G.J., *J. Phys. Chem. B* **2000**, 104, p. 11805.
6. Riley, K., Jankowiak, R., Rätsep, M., Small, G.J., Zazubovich, V., *J. Phys. Chem. B* **2004**, 108, p. 10346.
7. Brixner, T., Stenger, J., Vaswani, H. M., Cho, M., Blankenship, R. E., Fleming, G. R., *Nature* **2005**, 434, p. 625.
8. Förster, Th., *Ann. Phys.* [Series 6] **1948**, 2, p. 55.
9. Levine, Ira N. *Quantum Chemistry,* 5th ed.; Prentice Hall: New Jersey, 2000; p. 96.
10. Davydov, A.S., *Theory of Molecular Excitons*; Plenum: New York, 1971.
11. Reddy, N.R.S., Picorel, R., Small, G.J., *J. Phys. Chem.* **1992**, 96, p. 6458.
12. Rahman, T.S., Knox, R.S., Kenkre, V.M., *Chem. Phys.* **1979**, 44, p. 197.
13. Kühn, O., Renger, T., May, V., Voigt, J., Pullerits, T., Sundström, V., *Trends in Photochem. Photobiol.*; 1997; Vol. 4, p. 213.
14. Dexter, D.L., *J. Chem. Phys.* **1953**, 21, p. 836.

32. Elliot, R.I., *Phys. Rev.* **1957**, 108, p. 1384.

33. van Amerongen, H., Valkunas, L., van Grondelle, R., *Photosynthetic Excitons*; World Scientific Publishing: New York, 2000; p. 50-71.,

34. Kasha, M., Rawls, H.R., El-Bayoumi, M.A., *Pure Appl. Chem.* **1965**, 11, p. 371.

35. Jankowiak, R., Hayes, J.M., Small, G.J., *J. Phys. Chem. B* **2002**, 106, p. 8803.

36. Merry, S.A., Kamazaki, S., Tachibana, Y., Joseph, D.M., Porter, G., Yoshoara, K., Barber, J., Durrant, J.R., Klug, D.R., *J. Phys. Chem.* **1996**, 100, p. 10469.

37. Leegwater, J.A., Durrant, J.R., Klug, D.R., *J. Phys. Chem.* **1997**, 101,1, p. 7205.

38. Louwe, R.J.W., Vrieze, J., Hoff, A.J., Aartsma, T.J., *J. Phys. Chem. B* **1997**, 101, p. 11273.

39. Drenth J., *Principles of Protein X-Ray Crystallography;* Springer-Verlag: New York, 1999.

40. McDermott, G., Prince, S.M., Freer, A.A., Hawthornthwaite-Lawless, A.M., Papiz, M.Z., Cogdell, R.J., Isaacs, N.W., *Nature* **1995**, 374, p. 517.

41. Ferreira, K.N., Iverson, T.M., Maghlaoui, K., Barber, J., Iwata, S., *Science* **2004**, 303, p. 1831.

42. Jordan, P., Fromme, P., Witt, H.T., Klukas, O., Saenger, W., Krauss. N., *Nature* **2001**, 411, p. 909.

43. Loll, B., Kern, J., Saenger, W., Zouni, A., Biesiadka, J., *Nature* **2005**, 438, p. 1040.

44. Englman, R., *Nonradiative Decay of Ions and Molecules in Solids*; North-Holland: Amsterdam, 1979.

CHAPTER 3 – HOLE-BURNING AND SINGLE-MOLECULE SPECTROSCOPY

3.1 Spectral Lineshape Theory

Optical excitation of a molecule involves absorption of a quantum of light energy which promotes an electron from a ground state (E_g) to a higher quantized electronic energy level (E_{ex}). This excited electron can then return to the ground electronic state by emitting a photon or through radiationless energy decay. Since this excitation-decay process is quantum mechanical in nature, the Heisenberg uncertainty principle (H.U.P.) must be satisfied. The familiar form of H.U.P. is given by

$$\Delta x \Delta p \geq \frac{h}{2\pi} \tag{3.1}$$

where x is the position of the electron, p is its' momentum, and h is Planck's constant [1]. However, for optical spectroscopic processes, this relation can be recast in a more useful form as

$$\Delta E \Delta t \geq \frac{h}{2\pi} \tag{3.2}$$

where E is the energy of the electron and t is the time the electron spends at this particular energy [1]. It can be seen then that when the electron is promoted to a higher quantum energy level, the energy cannot be precisely known. Along with this, the time that this electron spends in this higher energy level cannot be precisely known; so to determine either the energy or time of a particular transition more precisely sacrifices the accuracy of the other. Therefore, the spectral lineshape of an optical transition is necessarily broadened by this condition, which is called *uncertainty or homogeneous broadening* [2].

This is often referred to as the *natural or homogeneous lineshape* of an optical transition (see Fig. 1).

For guest-host systems, such as molecular impurities in solid-state matrices (e.g. crystals, glasses, proteins), the homogeneous linewidth of an optical transition for a guest molecule at the zero point temperature (T = 0) has a characteristic time, referred to as the *energy relaxation time.* From Eq. 3.2, this relationship can be expressed as [3]

$$\Gamma(0) = \frac{1}{2\pi\, cT_1} \tag{3.3}$$

where $\Gamma(0)$ is the homogeneous linewidth in cm^{-1} at T = 0, c is the speed of light, and T_1 is the relaxation time. Unlike gas-phase optical transitions, Doppler broadening is not present since the guest molecule is attached to mass of the host matrix [3]. At T = 0, the homogeneous linewidth is appreciably narrow (10^{-4}-10^{-3} cm^{-1}) with a relaxation time of $T_1 \approx 10^{-7}$-10^{-8} s [3]. At $T \neq 0$, the homogeneous lineshape begins to broaden due to dephasing processes induced by thermally activated phonon modes of the host matrix.

The dephasing induced by phonons results from quasi-elastic scattering of a phonon by the molecular impurity, which changes the phonon's direction of propagation and a negligible change to its energy. For the impurity, this scattering results in a change in the phase of the excited electronic state wavefunction so that the time dependent part, $\exp(iE_{ex}t/\hbar)$, acquires an additional random phase component, δ, and changes to $\exp[(iE_{ex}t/h)+i\,\delta]$ [3]. Consequently, the lifetime of the excited quantum state is shortened, and the spectral linewidth carries additional uncertainty broadening. Therefore, at $T \neq 0$ the homogeneous linewidth must be described in terms of the energy relaxation and dephasing times:

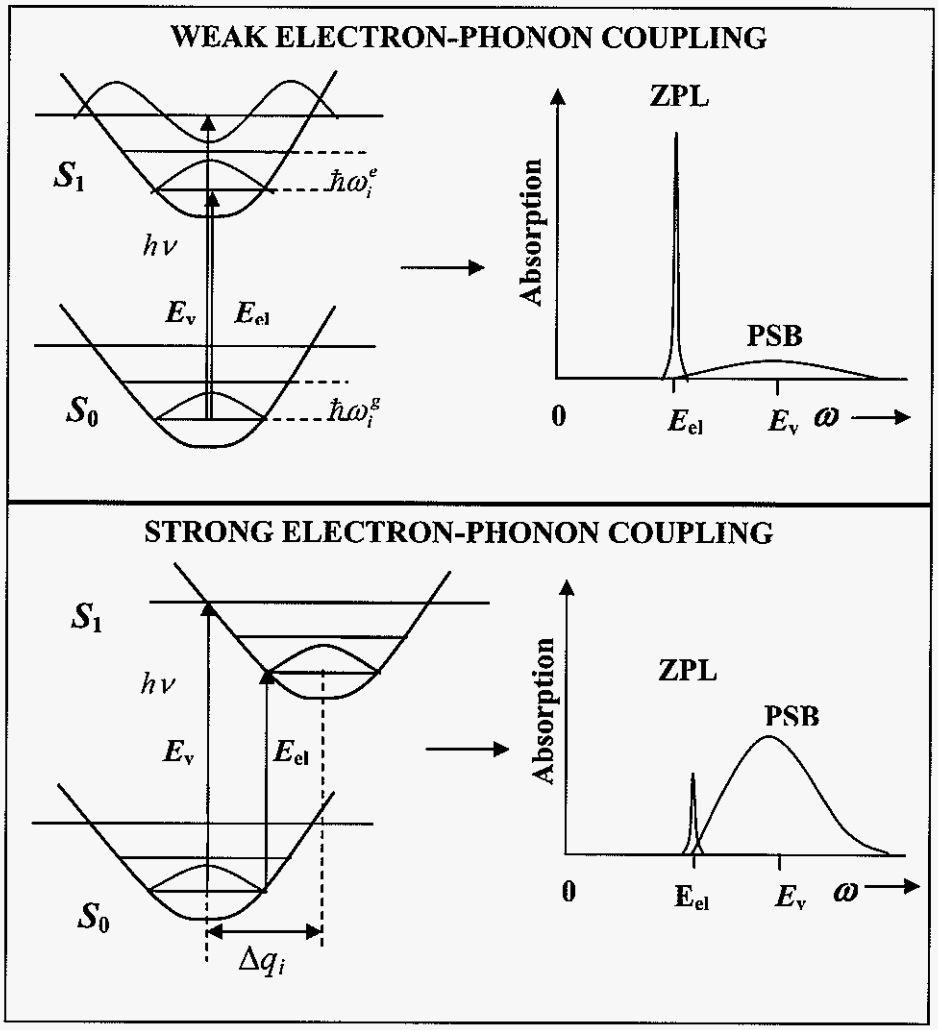

Figure 2. Schematic of the electron-phonon coupling of a guest impurity molecule in a low temperature solid host matrix via the Franck-Condon principle [9]. After excitation by $h\nu$, the molecule makes a transition from the ground electronic state, S_0, to the excited electronic state, S_1. The lattice coordinate displacement, Δq, determines the overlap between the ground and excited state vibrational wavefunctions; the stronger the overlap, the stronger the PSB feature. E_{el} and E_v represent the pure electronic and vertical transition energies, respectively. $h\omega_i^g$ and $h\omega_i^{ex}$ are the ground and excited state vibrational energy levels, respectively. [9]

$$\alpha = \exp(-S) \ , \tag{3.7}$$

where S is the dimensionless Stokes shift (also known as the Huang-Rhys factor) and is expressed as [11]:

$$S(T=0) = \frac{M_i \omega_i}{2\hbar} \sum_i (\Delta q_i)^2 \ . \tag{3.8}$$

In Eq. 3.8, M and ω_i are the reduced mass and frequency of the phonon mode i, respectively, and Δq_i is the change in equilibrium of lattice normal coordinate q_i. From Eq. 3.8, we see that $S \propto (\Delta q_i)^2$. Thus, S can be used to characterize the strength of the electron-phonon coupling. In general, electron phonon coupling is weak when $S < 1$. For $S > 1$, the electron-phonon coupling is strong [6, 12].

The DWF is temperature dependent. It decreases rapidly and, usually, monotonically as temperature increases, i. e. increasing temperature results in a rapid decease of ZPL intensity. The temperature dependent DWF is given by [13]:

$$\alpha(T) = \exp\left[-\sum_i^N S(2\bar{n}_i + 1) \right] , \tag{3.9}$$

where thermal occupation number, $\bar{n}_i = [\exp(\hbar\omega_i / kT) - 1]^{-1}$, is the average number of phonons of mode i at temperature T. $\alpha(T)$ reaches its maximum value at very low temperatures (T $\leq$ 10 K for most organic glasses).

3.2 Inhomogeneous Broadening

The preceding section discussed homogeneous lineshapes for a *single* impurity molecule in a host matrix. An ensemble of impurity molecules, however, will show a different characteristic spectrum. If the host matrix is not perfectly ordered so that each molecule experiences an identical environment, each molecule will experience a *different*

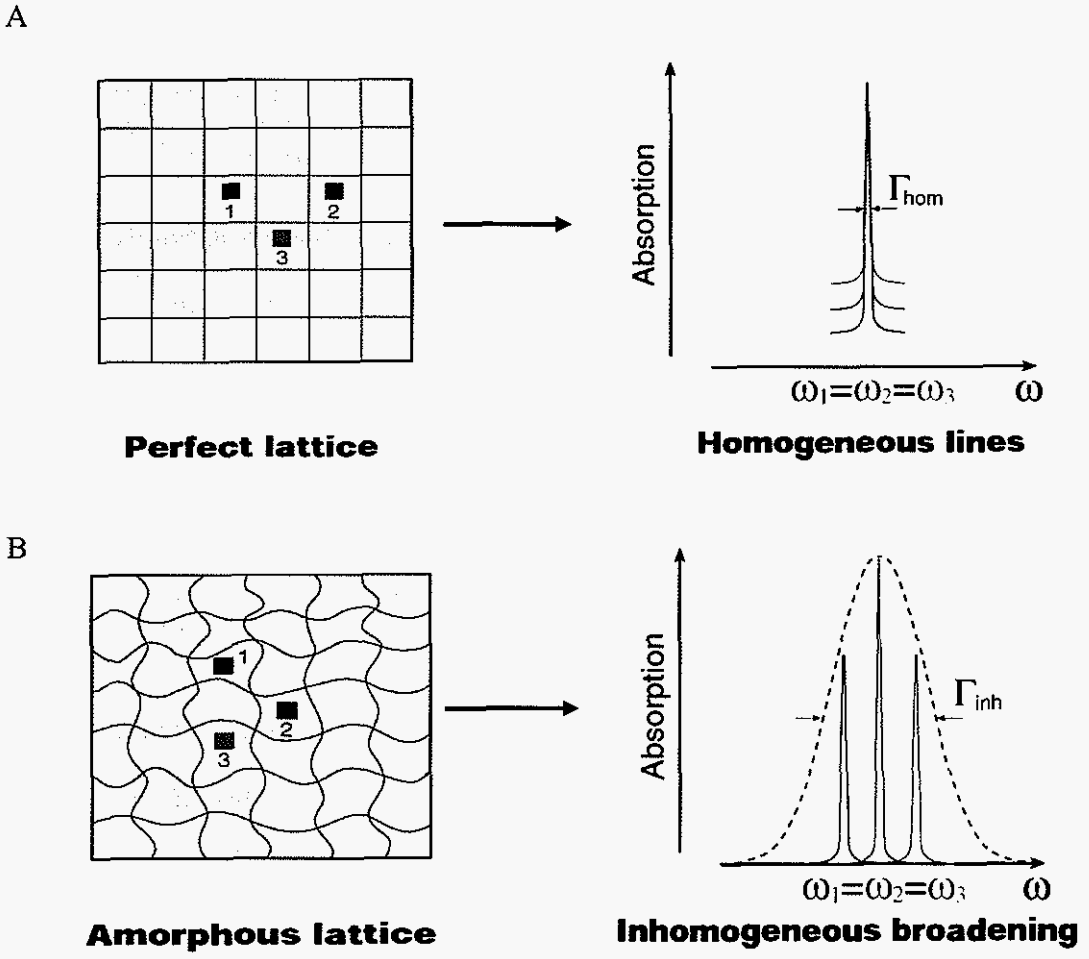

Figure 3. Schematic of homogeneous vs. inhomogeneous broadening. In frame (A), guest impurity molecules are in a perfect host lattice. Homogeneous lines (Γ_{hom}) overlap, resulting in an absorption spectrum with a linewidth = individual ZPL. In frame (B), guest impurity molecules are in a disordered host lattice, so that each impurity molecule absorbs at different frequency. This leads to a distribution of ZPL absorption frequencies and thus, the impurity absorption band is *inhomogeneously broadened.*

The basic physical principles of hole-burning (HB) are quite straightforward. To burn a spectral hole, a narrow bandwidth laser (λ_B) is used to excite a small subset of impurity molecules, which can be excited via their ZPLs in an inhomogeneously broadened absorption band. When these molecules are optically excited, they are then photophysically or photochemically transformed so that when they return to their ground electronic state, they no longer absorb at their original frequency. This leaves the inhomogeneous absorption band with a "hole" that has a shape that reveals the ZPL and PSB structure of these selected molecules (see Fig. 4). For sufficiently narrow laser linewidths, only the homogeneous lines that absorb at the exact same frequency will be "burned", thereby revealing the hidden individual homogeneous lineshapes in the inhomogeneously broadened band [38].

The different photophysical and photochemical pathways that result in a spectral hole determines the particular hole burning method. In *photochemical hole-burning* (PHB) *spectroscopy* [3, 27, 29-32], there is a photoreaction (such as tautomerization, bond breaking, and isomerization) of the impurity molecules in the excited electronic state so the chemical identity changes when the molecules return to the ground electronic state. The molecules then no longer have the same optical properties and do not absorb at the original excitation frequency. In *nonphotochemical hole-burning* (NPHB) *spectroscopy* [3, 35, 38], the host-guest matrix undergoes structural rearrangements when the impurity molecules are optically excited [40]. When the photochemically stable impurity molecules return to the ground electronic state the local nanoenvironment is different resulting in an energy shift of the impurity molecules, resulting in a spectral hole. Most commonly, NPHB is

observed in low temperature amorphous systems (glasses, polymers, and protein hosts) because of their inherent configurational host-guest interactions.

Unlike crystals whose low temperature properties are determined by phonons, glasses and proteins are determined by a different low temperature excitation, two-level systems (TLS) [35, 41, 42]. TLS are atoms or groups of atoms that can occupy different energetic configurations. It is the coupling of the impurity molecules to these TLS that accounts for the phenomenon of NPHB and is shown by a scheme of TLS transitions coupled to an impurity (extrinsic two-level system, TLS_{ext}) in Fig. 5 [40, 43, 44]. The superscripts α and β label the ground and excited electronic states of the probe. It is considered that excitation of the zero-phonon transition of a chromophore at frequency ω_B occurs in the left well, and is followed by a tunneling process in the excited state. The hole burning process of the chromophore competes with the relaxation to the ground state as depicted on the right well. The left to right relaxation that takes place in the excited electronic state leads to a blue-shifted anti-hole.

Based on optical dephasing studies [43, 45], it was suggested that for hole-burning two types of TLS - extrinsic (TLS_{ext}) and intrinsic (TLS_{int}) – are important. TLS_{ext} are associated with the impurity molecule and its inner shell of solvent molecules. In NPHB, the TLS_{ext} are responsible for the initiation of the hole formation. TLS_{int} of the host are connected with the excess free volume of glasses [46]. It is the coupling of the impurity molecules to the TLS_{int} and low frequency phonon modes that are responsible for optical dephasing in glassy solids. When the impurity molecule is optically excited, this triggers the rearrangement of the host environment, which then initiates the phonon-assisted tunneling process that leads to hole formation. Therefore, it is the

phonon-assisted tunneling in TLS_{ext}^{β} that is the rate-determining step in NPHB. The TLS_{ext}^{β} energy diagram in Fig. 5 depicts the situation where phonon-assisted tunneling in the excited state involves phonon emission and the anti-hole site absorbs at higher energy of ω_B. There are seven other energy level schemes [43]. Four of the eight lead to blue-shifted anti-hole sites, whereas the other four lead to red-shifted sites. Four of the schemes involve phonon absorption; the other four involve phonon emission. Extensions beyond the TLS model have also been made [48]; Shu and Small have proposed multi-level systems (MLS) in glasses and proteins, where several energetic configurations are present to further explain the NPHB phenomenon [43, 44].

Both PHB and NPHB are referred to as persistent hole burning methods, since the holes can be observed on an experimental timescale longer than it takes to burn them. This is in contrast to *transient spectral hole-burning*, where the holes can only be observed an a timescale equal to or shorter than the experimental timescale it takes to burn them [49]. In transient spectral hole burning, (or *triplet bottleneck hole-burning* (TBHB)), the triplet state is used as a reservoir to store excited impurity molecules in resonance with the laser line. While the impurity molecules are pumped into the triplet state, the absorption signal change can be measured with a spectrometer [49], or by using a reference laser beam to monitor the lifetime of the transient hole [50].

In particular, PHB, NPHB, and TBHB are powerful methods for determining the low temperature excitation/energy transfer properties of photosynthetic pigment protein complexes, whose spectra are inhomogeneously broadened due to intrinsic structural disorder of the protein matrix [15, 35, 38]. These spectroscopies can reveal important information, such as: (a) the inhomogeneous broadening of Γ_{inh} of

field $f\Delta\mu$ shifts are important because they can separate the excitonic states of closely spaced Chl molecules that are strongly coupled and possess charge transfer character [61, 68].

For high pressure hole burning experiments, the linear pressure shift rates of the ZPH (R_p) for strongly coupled Chl molecules are large ($R_p > \sim 0.2$ cm^{-1}/MPa), compared to the ZPH shift rates for excitations localized on a single Chl pigment molecule ($R_p \sim$ 0.05 to -0.15 cm^{-1}/MPa), and thus can be used to separate and characterize excitonic states. The linear pressure shift rates of ZPHs can also be used to identify closely spaced excited states that cannot be easily resolved based on their hole burning characteristics [62, 63].

Several formalisms for the theoretical modeling of HB spectra have been developed [35, 69, 70], with one such formalism developed by Hayes and Small [70]. This has been successfully used to simulate low temperature spectral holes of impurity doped glasses such as APT in glassy water and photosynthetic complexes such as the bacterial RC, photosystem I and II of cyanobacteria, and the FMO antenna complex [19, 62, 71, 72]. By using this master equation, the absorption at Ω after burning with a laser at ω_B for time t at the low temperature limit is given by

$$A(\Omega,t) = \exp(-\sum_k S_k)\prod_k \sum_{R=0}^{\infty}\left(\frac{S_k^R}{R!}\right)\int d\omega\ G(\omega)\exp^{-\sigma P\phi t L(\omega_B-\omega)}\, l_{R,k}(\Omega-\omega-R\omega_k)\ , \quad (3.12)$$

where $G(\omega)$ is the inhomogeneous distribution function introduced previously, σ is the integrated absorption cross section of the impurity molecule (cm^2), P is the photon flux in number of photons (cm^{-2} s^{-1}), and S_k is the Huang-Rhys factor of the kth phonon. ϕ is the hole-burning quantum yield that is given by [73]

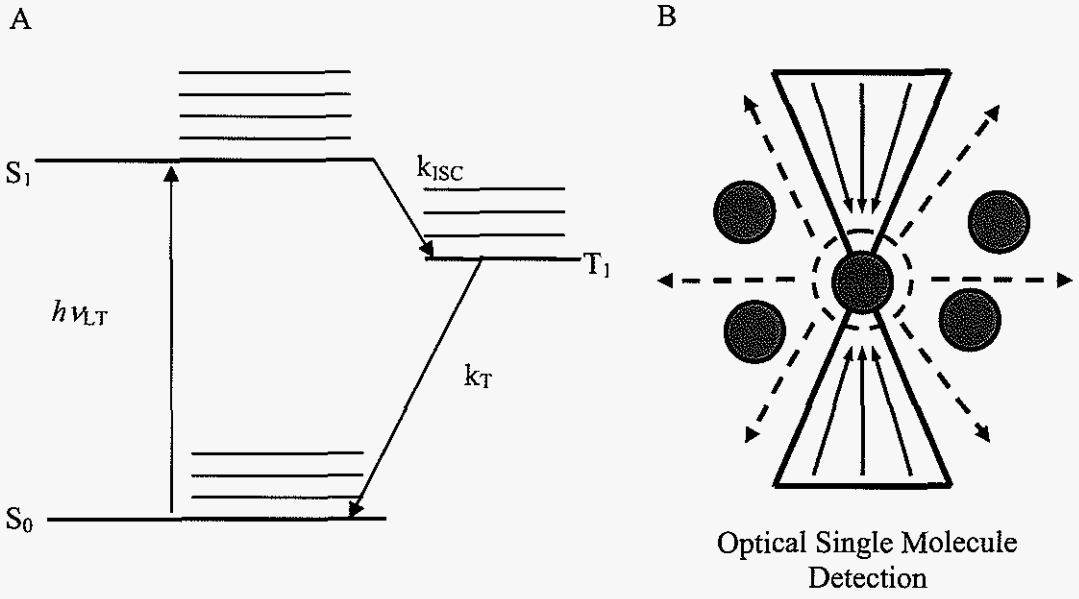

Figure 6. Energy level scheme (A) and illustration (B) of optical fluorescence single-molecule spectroscopy detection [97]. In frame (A), the molecule is excited from the zero point ground to the zero point excited electronic (0-0) transition at low temperatures, $h\nu_{LT}$, so there is no excitation from or into vibrational levels, which will cause optical dephasing. It is also advantageous to have a low intersystem cross rate, k_{ISC}, and a high triplet decay rate, k_T, so the molecule does not enter dark states where is does not fluoresce. In frame (B), a single molecule is detected by focusing the excitation profile (solid arrows), so that only one molecule is resonance, and then detecting the emitted fluorescence (dashed lines).

techniques have been successfully used for single molecule detection such as near-field optical scanning microscopy [93], confocal microscopy [94], and far-field techniques such as epiflourescence and total internal reflection microscopy [95, 96].

After this, the most challenging task for achieving SMS is to optimize the signal-to-noise ratio (SNR). For single molecule detection (using fluorescence excitation) in a solid, the SNR can be approximated by the following equation [97, 98]:

$$\mathrm{SNR} = \frac{D\phi_{\mathrm{F}}\left(\frac{\sigma^{\mathrm{P}}}{A}\right)\left(\frac{P_0}{h\nu}\right)\tau}{\sqrt{\frac{\left(D\phi_{\mathrm{F}}\sigma^{\mathrm{P}}P_0\tau\right)}{Ah\nu} + C_{\mathrm{b}}P_0\tau + N_{\mathrm{d}}\tau}} \tag{3.15}$$

where D is the overall efficiency for the detection of emitted photons (see [98, 99] for detailed description), ϕ_{F} is the fluorescence quantum yield, σ^{P} is the peak absorption cross-section, P_0 is the laser power, A is the focal spot area, $h\nu$ is the photon pump energy, τ is the detector counting interval, N_{d} is the dark count rate, and C_{b} is the background count rate per Watt of excitation power. In Eq. 3.15, the numerator represents the peak detected fluorescence counts from one molecule in time interval τ while the three terms in the denominator represent shot noise contributions from the emitted fluorescence, background, and dark signal, respectively.

According to Eq. 3.15, to maximize the SNR, the experimental conditions should be optimized for the smallest possible focal volume containing the probe molecule, thereby minimizing the background signal. In addition, the chosen probe molecule should (a) ideally have a large peak absorption cross-section, (b) high photostability and fluorescence quantum yield, (c) low triplet bottleneck probability, and (d) illumination

proportional to τ_2). Therefore, a narrow ZPL linewidth at low temperature gives a large peak absorption cross-section [3, 98].

In addition, the impurity molecule should be photostable and show weak hole burning at the excitation laser frequency. Since spectral hole burning causes the molecule to change its resonance frequency, it is necessary to provide sufficient time averaging of the single-molecule signal before it changes appreciably or moves to another spectral position. The fluorescence quantum yield of the molecule should be high as well, i.e. approach unity. The fluorescence quantum yield, ϕ_F, is given by [97]:

$$\phi = \frac{k_{\text{rad}}}{k_{\text{rad}} + k_{\text{nonrad}}} = \frac{\tau_F}{\tau_{\text{rad}}}, \tag{3.19}$$

where k_{rad} is the radiative rate (Einstein A coefficient), k_{nonrad} is the sum of all nonradiative rates (e.g. internal conversion, intersystem crossing), τ_F is the excited state lifetime, and τ_{rad} is the radiative lifetime [75]. The best fluorescing molecules are those with rigid structures that will decay via photon emission instead of non-radiatively through vibrational or rotational coupling. Strongly emitting molecules can have lifetimes that are on the order of ns, with a maximum photon emission rate of $\sim 10^8$ s^{-1}.

Optical saturation during excitation should also be avoided, as saturation leads to excess background signal and loss of absorption intensity since the molecule cannot efficiently decay back to the ground state. For organic molecules, saturation of the optical transitions becomes evident when the laser power $P_{laser} \geq 1$ W cm^{-2}. The dependence of the emission rate $R(I)$ of an excited molecule on the saturation intensity, I_S, is given by the following expression [97, 98]:

$$R(I) = R_\infty \frac{I / I_S}{(1 + I / I_S)} \tag{3.20}$$

$$I_S = \frac{h\nu k_{21}}{2\sigma^P}\left[\frac{1+(k_{ISC}/k_{21})}{1+(k_{ISC}/2k_T)}\right]. \quad (3.24)$$

In Eq. 3.24, the factor outside the brackets represents the saturation intensity if there was no triplet bottleneck, giving an upper limit for the saturation intensity. According to this equation, in order to minimize the triplet bottleneck probability, ideal impurity molecules should be those which give small values of k_{ISC} and large values of k_T. Commonly, organic rigid, planar aromatic molecules, such as chlorin pigment molecules, satisfy these requirements [74, 75].

3.3 SMS Experimental System

While many optical techniques for SMS have been developed (see above), epiflourescence and confocal microscopy detection schemes remain ubiquitous for SMS due their excellent combination of spatial and spectral selectivity [74, 75, 97]. For the single molecule experiments presented in this dissertation, a unique low temperature confocal microscopy experimental system was developed for detection of single photosynthetic complexes.

The optical system was based on a home-built confocal microscope with a Newport 60x 0.85 NA achromatic objective attached to the sample holder inside an immersion liquid helium cryostat (Janis). In order to reduce sample movements due to temperature expansion, the rod of the sample holder was made from fused quartz. The sample was moved in relation to the objective along the objective axis using an electromagnet with two parallel coils, one superconducting (for T < 7K) and the other made from copper wire. A computer-controlled scanning mirror was used to move the focal spot across the sample plane. Excitation was performed with a Coherent CR-699 laser with Exciton LD-688 dye (650-720 nm), and with intra-cavity etalons removed,

based on our experience (unpublished results), the photosynthetic complexes embedded in dry polymer films are disrupted compared to those studied in typical bulk experiments. Samples were then placed in a cold (< 0° C), dark, oxygen-free cryostat and the temperature was lowered to liquid helium temperature in about 20 minutes. Experiments were performed at 10 K in helium gas or at 2 K in superfluid helium. To avoid sample degradation, all room-temperature sample-handling procedures were performed in dim light as quickly as possible.